# The harmonic balance method with arc-length continuation in blade-tip/casing contact problems

Yann Colaïtis, Alain Batailly

POLYTECHNIQUE MONTRÉAL
UNIVERSITÉ D'INGÉNIERIE

LABORATOIRE D'ANALYSE VIBRATOIRE ET ACOUSTIQUE

# The harmonic balance method with arc-length continuation in blade-tip/casing contact problems

Y. Colaïtis[1], A. Batailly

**Abstract**

This article presents a Harmonic Balance Method-based numerical strategy to provide a qualitative numerical characterization of a compressor blade's dynamics when structural contacts occur with the surrounding casing. The mitigation of the Gibbs phenomenon follows a two-pronged approach: (1) a regularization of the unilateral contact law and (2) the adjustment of the Fourier coefficients by means of a Lanczos filtering technique. In order to validate the proposed approach, it is first applied to an academic cantilever rod undergoing unilateral contact constraints. An in-depth comparative analysis of the obtained results—with an emphasis on displacements, contact forces and velocities—with respect to a time integration-based reference numerical strategy underlines the relevance and accuracy of the proposed methodology. The latter is then applied to the vibration analysis of an industrial compressor blade: NASA rotor 37. For a given contact configuration, obtained results are thoroughly compared to those obtained with a previously published time integration-based numerical strategy with a distinct contact treatment algorithm. Particular attention is paid to demonstrate the accuracy of the methodology for the prediction of displacements, contact forces, velocities as well as stress fields within the blade. Notably, it is evidenced that the proposed methodology, contrary to the reference time integration-based numerical strategy, is able to capture the exact location of the blade's nonlinear resonance.

**Keywords**

harmonic balance method; numerical continuation; blade-tip/casing contacts; rubbing interaction; rotor/stator interaction; compressor blade

1 - Department of Mechanical Engineering, École Polytechnique de Montréal, P.O. Box 6079, Succ. Centre-Ville, Montréal, Québec, Canada H3C 3A7

# Application de la méthode de l'équilibrage harmonique couplée à une continuation par longueur d'arc aux problèmes de contact aube/carter

Y. Colaïtis[1], A. Batailly

**Résumé**

Cet article présente une stratégie numérique basée sur la méthode de l'équilibrage harmonique visant à fournir une caractérisation numérique qualitative de la dynamique d'une aube de compresseur lorsque des contacts structurels se produisent avec le carter environnant. L'atténuation du phénomène de Gibbs repose sur une double approche : (1) une régularisation de la loi de contact unilatéral et (2) l'ajustement des coefficients de Fourier au moyen d'une technique de filtrage de Lanczos. Afin de valider l'approche proposée, celle-ci est d'abord appliquée à un modèle académique de barre encastrée/libre soumise à des contraintes de contact unilatéral. Une analyse comparative approfondie des résultats obtenus–mettant l'accent sur les déplacements, les efforts de contact et les vitesses–avec une stratégie numérique de référence basée sur l'intégration temporelle souligne la pertinence et la précision de la méthodologie proposée. Cette dernière est ensuite appliquée à l'analyse des vibrations d'une aube de compresseur industriel : le rotor 37 de la NASA. Pour une configuration de contact donnée, les résultats obtenus sont minutieusement comparés à ceux obtenus à l'aide d'une stratégie numérique de référence basée sur l'intégration temporelle publiée antérieurement, utilisant notamment un algorithme de gestion du contact distinct. Une attention particulière est accordée à la démonstration de la précision de la méthodologie en termes de prédiction des déplacements, des efforts de contact, des vitesses ainsi que des champs de contrainte à l'intérieur de l'aube. Il est notamment démontré que la méthodologie proposée, à la différence de la stratégie numérique de référence, est capable de localiser exactement la résonance non-linéaire de l'aube.

**Mots-clés**

méthode de l'équilibrage harmonique; continuation numérique; contacts aube/carter; frottement aube/carter; interactions rotor/stator; aube de compresseur

1 - Département de génie mécanique, École Polytechnique de Montréal, P.O. Box 6079, Succ. Centre-Ville, Montréal, Québec, Canada H3C 3A7

## 1 Introduction

Over the past decade, aircraft engine manufacturers have focused their research efforts on two promising avenues for designing cleaner and more efficient turbomachines: the reduction of operating clearances [1] and the use of novel and lighter materials [2]. The former yields a significant reduction of aerodynamic leakages, particularly in compressor stages, and the latter leads to lighter components and a possible increase of temperatures within high-pressure turbine stages [3]. While these improvements allow recent aircraft engines to operate more efficiently with a reduced environmental footprint, they also create new challenges for engineers and designers. In particular, certain phenomena, formerly only considered in accidental configurations [4], must now be accounted for in nominal operating conditions. This is notably the case for blade-tip/casing structural contacts [5, 6].

The prediction of these contact phenomena has been at the center of many research works [7] initiated by different manufacturers [8, 9, 10]. Blade-tip/casing contact was first introduced as an extension of previous research investigations on rotor/stator interactions with an emphasis on the shaft/bearing contact interface [11]. However, the repeated experimental observations of critical interactions involving a single blade [1, 12, 13]—with no significant shaft motion or casing vibration—motivated designers and researchers to focus specifically on the so-called rubbing interactions [13, 14]. A better understanding of these interactions is now considered critical by manufacturers in a context where: (1) the drive for reduced operating clearances unavoidably promotes structural contact events [6], and (2) impacted components that may now be made of lighter materials typically feature lower admissible stresses than titanium alloys [3] and may thus be damaged when contacts occur.

The extremely high cost associated to full-scale experimental setups makes it particularly important for manufacturers to have at their disposal accurate predictive numerical strategies [15]. However, the intricacy of the simulated interactions often makes it impossible to use commercial software packages [13]. From a practical point of view, while full 3D finite element models of the blade must be considered for the sake of accuracy, one must also account for casing wear, thermomechanics and contact management which yields cumbersome computation times. More fundamentally, from a theoretical point of view, there is no unified framework in which mechanical structures undergoing structural contacts may be comprehensively analyzed: while recent developments in nonlinear and nonsmooth dynamics [16] are promising, there remains a gap to be filled before considering industrial implementation of these theories. For all these reasons, manufacturers rely on academic collaborations to develop their own predictive numerical tools [8, 10].

In order to predict the vibration behavior of aircraft engine blades undergoing contact interactions, one may consider two distinct frameworks: (1) numerical time integration [17], and (2) frequency methods [18]. In the context of turbomachinery, frequency methods such as the Harmonic Balance Method (HBM) have long been used for the prediction of the nonlinear vibrations of shaft-disk systems. HBM is also extremely popular and well-suited for the analysis of blade friction damping [19, 20, 21] for instance. However, so far, frequency methods have very rarely been considered for the analysis of blade-tip/casing contacts [11, 22, 23], and only with phenomenological models. There are two limitations to the use of HBM for the simulation of blade-tip/casing contacts: on the one hand, experimental observations in the vicinity of critical speeds underlined the importance of transient phenomena that cannot be captured with HBM. On the other hand, blade-tip/casing contacts yield discontinuous velocity and acceleration fields for which a Fourier-based numerical strategy may be ill-suited due to the Gibbs phenomenon [24, 25]. This last observation motivated the development of other frequency methods relying on other basis of functions such as wavelets [26].

Contrary to frequency methods, numerical time integration does not rely on any assumption with respect to the type of solution: the simulated system may thus exhibit a periodic, quasi-periodic or chaotic behavior. It also advantageously provides insight on transient phenomena. Over the past years, several studies focusing on the numerical prediction of blade-tip/casing structural contacts demonstrated that numerical time integration methods can provide results in good agreement with experimental observations [5, 13, 6]. These results led to the first redesign of aircraft engine blades [27] featuring a greater robustness to contact interactions. The inherently nonlinear nature of mechanical systems undergoing contact interactions makes their vibration level highly dependent on initial conditions. Thus, acquiring a qualitative view of a blade's dynamics—which is essential to improve its design and to avoid costly maintenance operations—using numerical time integration would require to run a potentially infinite number of simulations considering all types of initial conditions. This is a key issue when considering numerical time

integration.

In the end, in addition to quantitative results provided by time integration, a true qualitative understanding of a blade's dynamics behavior as it undergoes structural contacts must be achieved in order to provide designers with the tools they need for developing blades robust to contact interactions.

Current industrial practice for the simulation of blade-tip/casing contacts relies on numerical time integration: for a given contact configuration, several simulations are carried out one after another, for different angular speeds. Put together, results of these simulations typically provide an interaction map such as the one depicted in Fig. 1a. In this example, the interaction map features the juxtaposition of the spectra obtained with a Fast Fourier Transform (FFT) of the blade's leading edge radial displacement over its last revolutions at each angular speed. It should be noted here that all simulations are carried out independently from one another assuming null initial conditions on the blade. The considered contact configuration features two privileged contact areas per revolution which explains why the frequency content is located along even engine orders. This example also illustrates the contact stiffening phenomenon as the maximum amplitude is found for an angular speed significantly higher than the linear prediction corresponding to the intersection of the first bending mode eigenfrequency and engine order four. In order to better

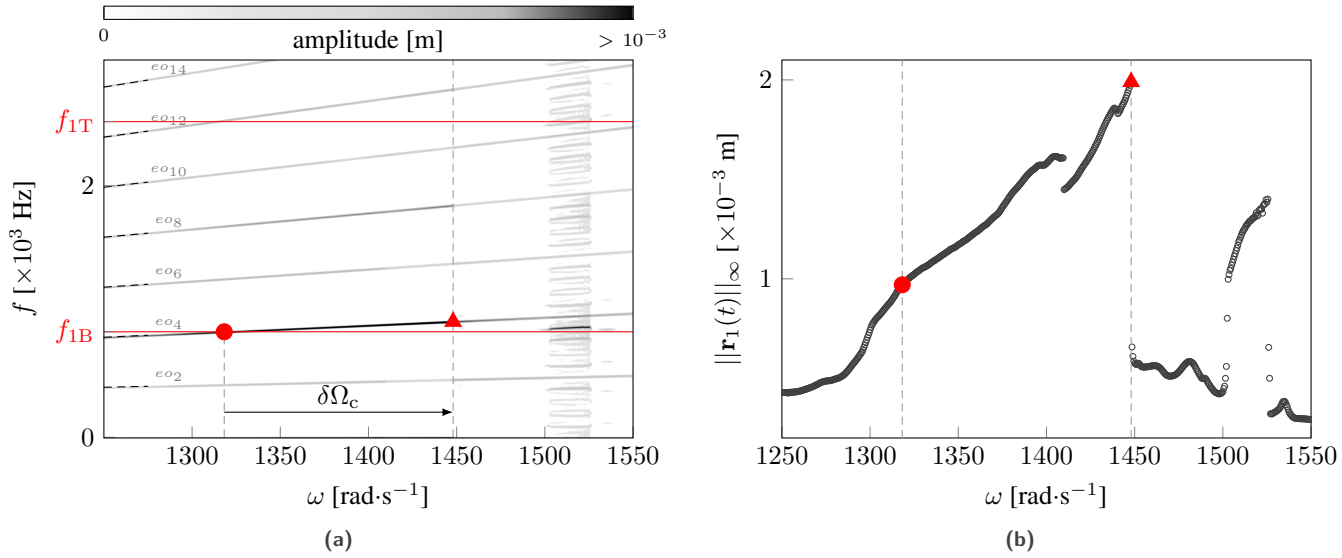


**Figure 1** – Numerical results for a test case of blade-tip/casing contact: (a) interaction map and (b) nonlinear frequency response curve.

visualize the jump in the amplitude response of the blade in the vicinity of the interaction speed, the infinity norm of the blade's leading edge radial displacement for the same simulations is depicted in Fig. 1b. This plot underlines the blade's sophisticated dynamics through out the angular speed range of interest since several jumps of amplitude can be observed.

The results depicted in Figs. 1a and 1b are consistent with the intricate dynamics of nonlinear mechanical systems but also clearly reveal that numerical time integration only provides a glimpse of it: jumps of amplitude are clear indications that numerical time integration does not capture certain solutions. More importantly, there is no way for designers to ensure that the predicted nonlinear resonance is indeed accurate since there could be higher amplitude solutions that are not captured with the selected initial conditions.

This paper presents a numerical methodology based on the HBM to provide the missing qualitative counterpart of results obtained by numerical time integration for blade-tip/casing contacts such as those pictured in Fig. 1. This is the first time that a frequency method is used for the prediction of an industrial compressor blade nonlinear response to contact events along its tip. As a first step towards the development of a generic tool for the qualitative analysis of rubbing interactions, the focus is made on the interaction between a realistic aircraft engine blade and a perfectly rigid, yet distorted, casing. Abradable wear and thermomechanics are thus not accounted for in this study.

In the section 2 of the paper, the methodology is detailed with an emphasis on the contact model, model reduction and the employed strategy to mitigate the Gibbs phenomenon. An extensive validation of the proposed methodoloy is carried out in the section 3 of the paper on a numerically sensitive contact configuration between a rod and a rigid obstacle. Finally, in the section 4, the proposed methodology is applied on the full 3D finite element model of an industrial transonic compressor blade: NASA rotor 37.

## 2 Regularized-Lanczos harmonic balance method

The equation of motion of a $n$-degrees of freedom (dof) nonlinear mechanical system reads:

$$\mathbf{M}\ddot{\mathbf{x}} + \mathbf{C}\dot{\mathbf{x}} + \mathbf{K}\mathbf{x} + \mathbf{f}_{\text{nl}}(\mathbf{x}, \dot{\mathbf{x}}) = \mathbf{f}_{\text{ext}}(\omega, t) \tag{1}$$

where $\mathbf{M}$, $\mathbf{C}$, $\mathbf{K}$ are respectively the mass, damping and stiffness matrices, $\mathbf{x}$ is the displacement vector, $\mathbf{f}_{\text{nl}}$ represents the nonlinear forces and $\mathbf{f}_{\text{ext}}$ correponds to periodic excitation forces of angular frequency $\omega$. The overdots refer to derivatives with respect to time $t$.

### 2.1 The harmonic balance method

The HBM allows to solve Eq. (1) assuming that its solution $\mathbf{x}$ as well as forces $\mathbf{f}_{\text{nl}}$ and $\mathbf{f}_{\text{ext}}$ may be written as truncated Fourier series:

$$\begin{aligned}
\mathbf{x}(t) &\simeq \frac{1}{2}\mathbf{a}_0 + \sum_{j=1}^{H} \left[\mathbf{a}_j \cos(j\omega t) + \mathbf{b}_j \sin(j\omega t)\right] \\
\mathbf{f}_{\text{nl}}(\mathbf{x}, \dot{\mathbf{x}}) &\simeq \frac{1}{2}\mathbf{a}_0^{\text{nl}} + \sum_{j=1}^{H} \left[\mathbf{a}_j^{\text{nl}} \cos(j\omega t) + \mathbf{b}_j^{\text{nl}} \sin(j\omega t)\right] \\
\mathbf{f}_{\text{ext}}(\omega, t) &\simeq \frac{1}{2}\mathbf{a}_0^{\text{ext}} + \sum_{j=1}^{H} \left[\mathbf{a}_j^{\text{ext}} \cos(j\omega t) + \mathbf{b}_j^{\text{ext}} \sin(j\omega t)\right]
\end{aligned} \tag{2}$$

where $\mathbf{a}_j^{\alpha}$ and $\mathbf{b}_j^{\alpha}$, $\alpha = \{\cdot,\ \text{nl},\ \text{ext}\}$, are the unknown real Fourier coefficients respectively related to cosine and sine terms. Each of these coefficients are vectorial quantities:

$$\begin{cases}
\mathbf{a}_j^{\alpha} = \left[a_j^{\alpha,1},\ a_j^{\alpha,2},\ \ldots,\ a_j^{\alpha,n}\right] & \text{for } j \in [\![0..H]\!] \\
\mathbf{b}_j^{\alpha} = \left[b_j^{\alpha,1},\ b_j^{\alpha,2},\ \ldots,\ b_j^{\alpha,n}\right] & \text{for } j \in [\![1..H]\!]
\end{cases} \tag{3}$$

For the sake of clarity, all Fourier coefficients are gathered in $n(2H+1)$-dimensional vectors so that the following frequency domain variables may be defined:

$$\begin{aligned}
\tilde{\mathbf{x}} &= \left[\,\mathbf{a}_0,\ \mathbf{a}_1,\ \mathbf{b}_1,\ \ldots,\ \mathbf{a}_H,\ \mathbf{b}_H\,\right]^{\top} \\
\tilde{\mathbf{f}}_{\text{nl}} &= \left[\,\mathbf{a}_0^{\text{nl}},\ \mathbf{a}_1^{\text{nl}},\ \mathbf{b}_1^{\text{nl}},\ \ldots,\ \mathbf{a}_H^{\text{nl}},\ \mathbf{b}_H^{\text{nl}}\,\right]^{\top} \\
\tilde{\mathbf{f}}_{\text{ext}} &= \left[\,\mathbf{a}_0^{\text{ext}},\ \mathbf{a}_1^{\text{ext}},\ \mathbf{b}_1^{\text{ext}},\ \ldots,\ \mathbf{a}_H^{\text{ext}},\ \mathbf{b}_H^{\text{ext}}\,\right]^{\top}
\end{aligned} \tag{4}$$

Fourier series detailed in Eq. (2) may thus be written in a more compact form:

$$\begin{aligned}
\mathbf{x}(t) &= (\mathbf{T}_H \otimes \mathbf{I}_n)\,\tilde{\mathbf{x}} \\
\mathbf{f}_{\text{nl}}(\mathbf{x}, \dot{\mathbf{x}}) &= (\mathbf{T}_H \otimes \mathbf{I}_n)\,\tilde{\mathbf{f}}_{\text{nl}} \\
\mathbf{f}_{\text{ext}}(\omega, t) &= (\mathbf{T}_H \otimes \mathbf{I}_n)\,\tilde{\mathbf{f}}_{\text{ext}}
\end{aligned} \tag{5}$$

where $\otimes$ denotes the Kronecker product, $\mathbf{I}_n$ is the identity matrix of size $n$ and $\mathbf{T}_H$ stands for the Fourier basis in real form defined as:

$$\mathbf{T}_H = \left[\frac{1}{2},\ \cos(\omega t),\ \sin(\omega t),\ \ldots,\ \cos(H\omega t),\ \sin(H\omega t)\right] \tag{6}$$

Velocities and accelerations may then be written as:

$$\begin{aligned}\dot{\mathbf{x}}(t) &= (\dot{\mathbf{T}}_H \otimes \mathbf{I}_n)\tilde{\mathbf{x}} = \omega((\mathbf{T}_H\boldsymbol{\nabla}) \otimes \mathbf{I}_n)\,\tilde{\mathbf{x}} \\ \ddot{\mathbf{x}}(t) &= (\ddot{\mathbf{T}}_H \otimes \mathbf{I}_n)\tilde{\mathbf{x}} = \omega^2((\mathbf{T}_H\boldsymbol{\nabla}^2) \otimes \mathbf{I}_n)\,\tilde{\mathbf{x}}\end{aligned} \tag{7}$$

where $\boldsymbol{\nabla}$ is the global differential operator of $\mathbf{T}_H$ defined by:

$$\boldsymbol{\nabla} = \text{diagblock}(0,\ \boldsymbol{\nabla}_1,\ \ldots,\ \boldsymbol{\nabla}_j,\ \ldots,\ \boldsymbol{\nabla}_H) \quad \text{and} \quad \boldsymbol{\nabla}^2 = \boldsymbol{\nabla}\boldsymbol{\nabla} \tag{8}$$

with the elementary first order derivative matrix $\boldsymbol{\nabla}_j$:

$$\boldsymbol{\nabla}_j = j \begin{bmatrix} 0 & 1 \\ -1 & 0 \end{bmatrix} \text{ for } j \in [\![1..H]\!] \tag{9}$$

The substitution of displacements, velocities, accelerations and forces from Eqs. (5) and (7) into Eq. (1), followed by the balancing of harmonic terms with a Fourier-Galerkin projection yields the following $n(2H+1)$ nonlinear algebraic equations in the frequency domain:

$$\mathbf{R}(\tilde{\mathbf{x}}, \omega) = \mathbf{Z}(\omega)\tilde{\mathbf{x}} + \tilde{\mathbf{f}}_{\text{nl}}(\tilde{\mathbf{x}}) - \tilde{\mathbf{f}}_{\text{ext}}(\omega) = \mathbf{0} \tag{10}$$

where $\mathbf{Z}(\omega)$ is the so-called *global dynamic stiffness* matrix, a block diagonal matrix defined as follows:

$$\mathbf{Z}(\omega) = \omega^2\boldsymbol{\nabla}^2 \otimes \mathbf{M} + \omega\boldsymbol{\nabla} \otimes \mathbf{C} + \mathbf{I}_{2H+1} \otimes \mathbf{K} \tag{11}$$

Solutions of Eq. (10) may be found with an iterative procedure such as the Newton-Raphson method: starting from a well-chosen initial guess $\tilde{\mathbf{x}}^0$, a converged solution is obtained iteratively:

$$\tilde{\mathbf{x}}^{k+1} = \tilde{\mathbf{x}}^k + \Delta\tilde{\mathbf{x}}^k \quad \text{with} \quad \mathbf{R}^k_{,\tilde{\mathbf{x}}}\Delta\tilde{\mathbf{x}}^k = -\mathbf{R}^k \tag{12}$$

where $\mathbf{R}^k = \mathbf{R}(\tilde{\mathbf{x}}^k, \omega)$ is the residual at iteration $k$ and $\mathbf{R}^k_{,\tilde{\mathbf{x}}}$ is the jacobian matrix of the system with respect to $\tilde{\mathbf{x}}^k$:

$$\mathbf{R}^k_{,\tilde{\mathbf{x}}} = \frac{\partial \mathbf{R}}{\partial \tilde{\mathbf{x}}}(\tilde{\mathbf{x}}^k, \omega) = \mathbf{Z}(\omega) + \tilde{\mathbf{f}}_{\text{nl},\tilde{\mathbf{x}}} = \mathbf{Z}(\omega) + \frac{\partial \tilde{\mathbf{f}}_{\text{nl}}(\tilde{\mathbf{x}}^k)}{\partial \tilde{\mathbf{x}}} \tag{13}$$

Iterations are stopped once the convergence criterion has been met:

$$\frac{||\mathbf{R}(\tilde{\mathbf{x}}^k, \omega)||_2}{||\tilde{\mathbf{x}}^k||_2} \leq \varepsilon, \quad \varepsilon \in \mathbb{R}^*_+ \tag{14}$$

### 2.2 Path following continuation technique

As illustrated in Fig. 1, nonlinear mechanical systems typically exhibit a complex dynamic behavior. It is expected to find amplitude jumps during frequency sweeps which indicate that coexisting stable solutions may exist for a given angular frequency $\omega$. When used in combination with a continuation technique [18], the HBM becomes well-suited for predicting these multiple solutions. Continuation techniques rely on the fact that a good initial estimate for the computation of a solution of the system at a given angular frequency $\omega$ may be obtained from solutions previously computed in the vicinity of $\omega$, be it by lower or upper values. Among the available continuation techniques in the literature [28, 29]—arc-length, pseudo-arc-length (orthogonal), Moore-Penrose or the asymptotic numerical method—the arc-length continuation technique [18, 30] may be the most commonly used and is also considered in this study. This continuation technique is represented schematically in Fig. 2.

The arc-length continuation technique is based on a prediction-correction approach. In order to draw the Nonlinear Frequency Response Curve (NFRC) of the system, when solving Eq. 10, the search direction is constrained by the following parameterization $\mathcal{P}$:

$$\mathcal{P}(\tilde{\mathbf{x}}^k_{i+1}, \omega^k_{i+1}, s) = ||\tilde{\mathbf{x}}^k_{i+1} - \tilde{\mathbf{x}}_i||^2_2 + (\omega^k_{i+1} - \omega_i)^2 - \Delta s^2_{i+1} = 0 \tag{15}$$

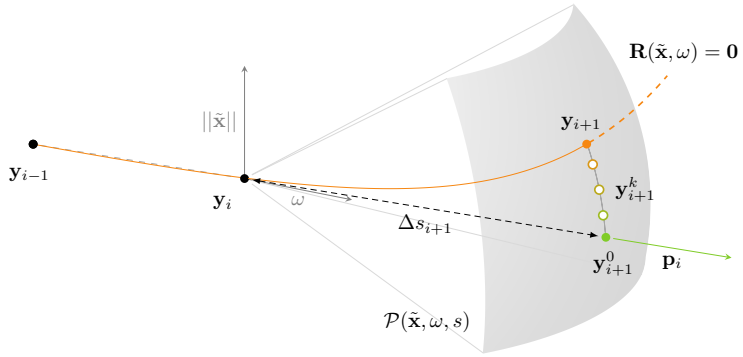


**Figure 2** – Principle of the arc-length continuation technique: known solutions (●), prediction (●) and new solution (●).

where $s$ is the curvilinear abscissa of the curve. As $\omega$ becomes an additional unknown, the size of the system to solve (10) is increased. Considering the arc-length parameterization, finding the solution:

$$\mathbf{y}_{i+1} = \left[\tilde{\mathbf{x}}_{i+1}, \omega_{i+1}\right]^\top \tag{16}$$

may thus be interpreted as enforcing the point $\mathbf{y}^k_{i+1}$ to lie at the intersection of the residual curve $\mathbf{R}(\tilde{\mathbf{x}},\omega)=\mathbf{0}$ and the surface of an hypersphere of radius $\Delta s$ centered on the previous solution $\mathbf{y}_i$. To this end, a prediction is made so that the iterative correction procedure benefits from a suitable initial guess in order to enhance the chances of successful convergence. This is achieved by using a predictor $\mathbf{p}$ that may be secant, tangent to the NFRC or obtained from a higher order extrapolation of the NFRC such as Lagrange polynomials [31].

In this study, a secant predictor is used as it was found to enhance the robustness of the methodology when considering contact nonlinearities. Based on last two found solutions $\mathbf{y}_{i-1}$ and $\mathbf{y}_i$, a predicted solution $\mathbf{y}^0_{i+1}$ at distance $\Delta s_{i+1}$ along the normalized secant direction is made to initiate the iterative correction procedure:

$$\mathbf{y}^0_{i+1} = \mathbf{y}_i + \Delta s_{i+1} \frac{\mathbf{y}_i - \mathbf{y}_{i-1}}{||\mathbf{y}_i - \mathbf{y}_{i-1}||_2} \tag{17}$$

Newton-Raphson subsequent iterations are then obtained by solving the augmented system:

$$\mathbf{y}^{k+1}_{i+1} = \mathbf{y}^k_{i+1} + \begin{bmatrix} \Delta\tilde{\mathbf{x}} \\ \Delta\omega \end{bmatrix} \quad \text{with} \quad \begin{bmatrix} \mathbf{R}_{,\tilde{\mathbf{x}}}(\mathbf{y}^k_{i+1}) & \mathbf{R}_{,\omega}(\mathbf{y}^k_{i+1}) \\ \mathcal{P}^\top_{,\tilde{\mathbf{x}}}(\mathbf{y}^k_{i+1}, s) & \mathcal{P}_{,\omega}(\mathbf{y}^k_{i+1}, s) \end{bmatrix} \begin{bmatrix} \Delta\tilde{\mathbf{x}} \\ \Delta\omega \end{bmatrix} = \begin{bmatrix} -\mathbf{R}(\mathbf{y}^k_{i+1}) \\ -\mathcal{P}(\mathbf{y}^k_{i+1}, s) \end{bmatrix} \tag{18}$$

where partial derivatives $\mathcal{P}_{,\tilde{\mathbf{x}}}$ and $\mathcal{P}_{,\omega}$ are defined by:

$$\mathcal{P}_{,\tilde{\mathbf{x}}}(\tilde{\mathbf{x}}^k_{i+1}, \omega^k_{i+1}, s) = 2\left(\tilde{\mathbf{x}}^k_{i+1} - \tilde{\mathbf{x}}_i\right) \quad \text{and} \quad \mathcal{P}_{,\omega}(\tilde{\mathbf{x}}^k_{i+1}, \omega^k_{i+1}, s) = 2\left(\omega^k_{i+1} - \omega_i\right) \tag{19}$$

and where $\mathbf{R}_{,\omega}$ the gradient of system 10 with respect to $\omega$ is given by:

$$\mathbf{R}_{,\omega} = \frac{\partial \mathbf{R}}{\partial \omega} = \mathbf{Z}_{,\omega}\tilde{\mathbf{x}} + \tilde{\mathbf{f}}_{\mathrm{nl},\omega} - \tilde{\mathbf{f}}_{\mathrm{ext},\omega} = \left(2\omega\boldsymbol{\nabla}^2 \otimes \mathbf{M} + \boldsymbol{\nabla} \otimes \mathbf{C}\right)\tilde{\mathbf{x}} + \frac{\partial \tilde{\mathbf{f}}_{\mathrm{nl}}(\tilde{\mathbf{x}},\omega)}{\partial \omega} - \frac{\partial \tilde{\mathbf{f}}_{\mathrm{ext}}(\omega)}{\partial \omega} \tag{20}$$

Solution of the augmented system given in Eq. (18) may be performed using a block elimination algorithm [32, 33] that takes advantage of the bordered structure of the left-hand side coefficient matrix. This technique advantageously prevents numerical difficulties that may arise from the singularity of the jacobian matrix $\mathbf{R}_{,\tilde{\mathbf{x}}}$ at turning points. It thus allows factorizing only $\mathbf{R}_{,\tilde{\mathbf{x}}}$, which is done with a partially pivoted LU decomposition.

Finally, an efficient automated angular frequency step adjustment procedure is key for a robust continuation technique. Such procedures greatly facilitate the following of a solution path. The one used in this article allows

to dynamically update the step $\Delta s_{i+1}$ depending on the success of the Newton-Raphson iterative procedure [28]. Between each consecutive converged solution, $\Delta s_{i+1}$ is updated according to the total number of iterations $k_i$ that were performed to obtain the previous $i$-th solution, so that:

$$\Delta s_{i+1} = \Delta s_i \, 2^{\frac{k_{\text{opti}} - k_i}{k_{\text{opti}}}} \tag{21}$$

where $k_{\text{opti}}$ is an optimal number of corrections *a priori* prescribed by the user. The value of this parameter mainly depends on the stopping criterion of the iterative solver. One may note that $\Delta s$ must be adequately bounded: if it is too large, the continuation may skip areas of interest or even generate numerical problem such as cyclic jumping between solution branches [29]. To the contrary, if $\Delta s$ is too small, it will lead to unnecessarily slow computations. Shall the iterative solver not converge within $k_{\text{opti}}$ iterations, the prediction distance will then be halved to obtain a new initial guess before relaunching the iterative solver.

## 2.3 Computation of nonlinear forces

### *2.3.1 Alternating frequency/time scheme*

While the expression of the external forcing $\tilde{\mathbf{f}}_{\text{ext}}$ may be known, nonlinear forces $\tilde{\mathbf{f}}_{\text{nl}}$ however explicitly depend on $\tilde{\mathbf{x}}$ and cannot be estimated *a priori*. To deal with this issue, an Alternating Frequency/Time (AFT) scheme [34] may be used. The AFT scheme—which is illustrated in Fig. 3—consists in using direct and inverse Discrete Fourier Transform (DFT) to evaluate in the time domain the expression of nonlinear forces $\mathbf{f}_{\text{nl}}(\mathbf{x}, \dot{\mathbf{x}})$ and their partial derivatives $\mathbf{f}_{\text{nl},\mathbf{x}}$, $\mathbf{f}_{\text{nl},\dot{\mathbf{x}}}$ and $\mathbf{f}_{\text{nl},\omega}$. These terms are then projected back onto the frequency domain to obtain $\tilde{\mathbf{f}}_{\text{nl}}$, $\tilde{\mathbf{f}}_{\text{nl},\tilde{\mathbf{x}}}$ and $\tilde{\mathbf{f}}_{\text{nl},\omega}$.

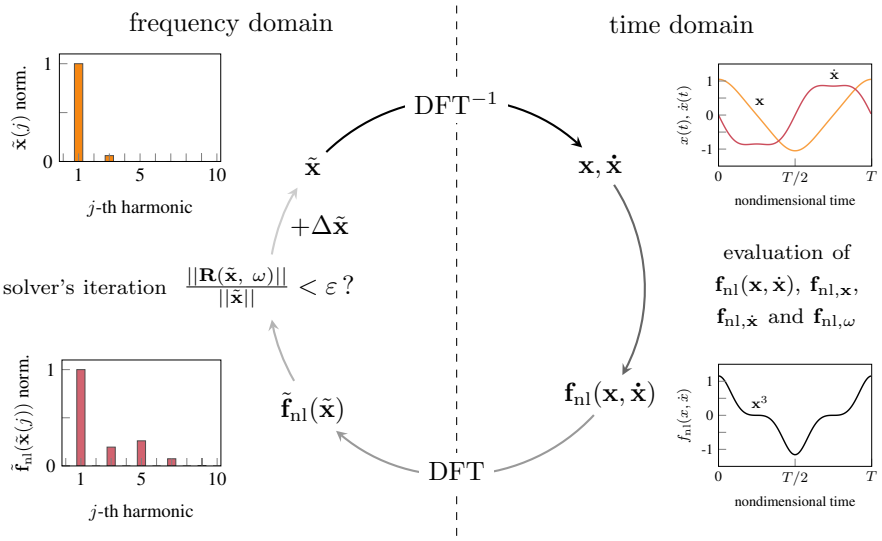


**Figure 3** – Illustration of the alternating frequency/time scheme.

In the time domain, $\mathbf{x}$ and $\mathbf{f}_{\text{nl}}$ are evaluated at $N$ time steps, $t_i = \frac{2\pi}{\omega}\frac{i}{N}$ for $i \in [\![0..N-1]\!]$, evenly distributed over one period $T$:

$$\begin{aligned} \mathbf{x} &= [\mathbf{x}_1, \dots, \mathbf{x}_n]^\top = [x_{1,0}, \dots, x_{1,N-1}, \dots, x_{n,0}, \dots, x_{n,N-1}]^\top \\ \mathbf{f}_{\text{nl}}(\mathbf{x}, \dot{\mathbf{x}}) &= [\mathbf{f}_1, \dots, \mathbf{f}_n]^\top = [f_{1,0}, \dots, f_{1,N-1}, \dots, f_{n,0}, \dots, f_{n,N-1}]^\top \end{aligned} \tag{22}$$

Displacement, velocity and acceleration fields in the time domain may be obtained using inverse DFT [35]:

$$\begin{aligned} \mathbf{x} &= \boldsymbol{\Gamma}\tilde{\mathbf{x}} \\ \dot{\mathbf{x}} &= \omega\boldsymbol{\Gamma}(\boldsymbol{\nabla} \otimes \mathbf{I}_n)\tilde{\mathbf{x}} \\ \ddot{\mathbf{x}} &= \omega^2\boldsymbol{\Gamma}(\boldsymbol{\nabla}^2 \otimes \mathbf{I}_n)\tilde{\mathbf{x}} \end{aligned} \tag{23}$$

with $\boldsymbol{\Gamma}$, the rectangular $(nN \times n(2H+1))$-dimensional inverse DFT matrix:

$$\boldsymbol{\Gamma} = \left[ \mathbf{I}_n \otimes \begin{bmatrix} 1/2 \\ \vdots \\ 1/2 \end{bmatrix} \quad \mathbf{I}_n \otimes \begin{bmatrix} \cos(\omega t_0) \\ \vdots \\ \cos(\omega t_{N-1}) \end{bmatrix} \quad \mathbf{I}_n \otimes \begin{bmatrix} \sin(\omega t_0) \\ \vdots \\ \sin(\omega t_{N-1}) \end{bmatrix} \quad \dots \right.$$
$$\left. \dots \quad \mathbf{I}_n \otimes \begin{bmatrix} \cos(H\omega t_0) \\ \vdots \\ \cos(H\omega t_{N-1}) \end{bmatrix} \quad \mathbf{I}_n \otimes \begin{bmatrix} \sin(H\omega t_0) \\ \vdots \\ \sin(H\omega t_{N-1}) \end{bmatrix} \right] \tag{24}$$

Conversely, frequency domain quantities may be obtained from their time domain counterparts through a DFT:

$$\begin{aligned} \tilde{\mathbf{x}} &= \boldsymbol{\Gamma}^{-1}\mathbf{x} \\ \tilde{\mathbf{f}}_{\mathrm{nl}} &= \boldsymbol{\Gamma}^{-1}\mathbf{f}_{\mathrm{nl}} \end{aligned} \tag{25}$$

where inverse $\boldsymbol{\Gamma}^{-1}$ is the direct DFT matrix and may be constructed as follows:

$$\boldsymbol{\Gamma}^{-1} = \frac{2}{N} \begin{bmatrix} \mathbf{I}_n \otimes & [1 & \dots & 1] \\ \mathbf{I}_n \otimes & [\cos(\omega t_0) & \dots & \cos(\omega t_{N-1})] \\ \mathbf{I}_n \otimes & [\sin(\omega t_0) & \dots & \sin(\omega t_{N-1})] \\ & & \vdots & \\ \mathbf{I}_n \otimes & [\cos(H\omega t_0) & \dots & \cos(H\omega t_{N-1})] \\ \mathbf{I}_n \otimes & [\sin(H\omega t_0) & \dots & \sin(H\omega t_{N-1})] \end{bmatrix} \tag{26}$$

The introduction of nondimensional time $\tau = \omega t$—or, in a discretized manner, $\tau_i = 2\pi \frac{i}{N}$ for $i \in [\![0..N-1]\!]$—in Eqs. (24) and (26) advantageously makes operators $\boldsymbol{\Gamma}$ and $\boldsymbol{\Gamma}^{-1}$ independent of the angular frequency $\omega$. This way, a single evaluation of these operators is required thus yielding significant gains in terms of computational efficiency.

### 2.3.2 Numerical considerations

The accuracy and the efficiency of the AFT procedure greatly depends on the number of time steps $N$. The theoretical lower bound value of $N$ is given by the Nyquist-Shanon criterion in order to prevent aliasing errors: $N \geq 2H+1$. However, the AFT scheme usually requires a much larger value of $N$. This is particularly true when considering strong nonlinearities such as those related to structural contact [29].

An accurate estimate of derivatives $\tilde{\mathbf{f}}_{\mathrm{nl},\tilde{\mathbf{x}}}$ and $\tilde{\mathbf{f}}_{\mathrm{nl},\omega}$ is essential to ensure the robustness of Newton type, gradient based, nonlinear solvers. Hence the efficiency of the AFT scheme is closely related to the derivation of the nonlinear forces [30]. Linearity of DFT operators $\boldsymbol{\Gamma}$ and $\boldsymbol{\Gamma}^{-1}$, and use of the chain rule, provide an efficient general analytic formulation of derivatives [21]:

$$\frac{\partial \tilde{\mathbf{f}}_{\mathrm{nl}}(\tilde{\mathbf{x}})}{\partial \tilde{\mathbf{x}}} = \frac{\partial \tilde{\mathbf{f}}_{\mathrm{nl}}}{\partial \mathbf{f}_{\mathrm{nl}}} \frac{\partial \mathbf{f}_{\mathrm{nl}}}{\partial \mathbf{x}} \frac{\partial \mathbf{x}}{\partial \tilde{\mathbf{x}}} + \frac{\partial \tilde{\mathbf{f}}_{\mathrm{nl}}}{\partial \mathbf{f}_{\mathrm{nl}}} \frac{\partial \mathbf{f}_{\mathrm{nl}}}{\partial \dot{\mathbf{x}}} \frac{\partial \dot{\mathbf{x}}}{\partial \tilde{\mathbf{x}}} = \boldsymbol{\Gamma}^{-1} \frac{\partial \mathbf{f}_{\mathrm{nl}}}{\partial \mathbf{x}} \boldsymbol{\Gamma} + \boldsymbol{\Gamma}^{-1} \frac{\partial \mathbf{f}_{\mathrm{nl}}}{\partial \dot{\mathbf{x}}} \boldsymbol{\Gamma}(\omega \boldsymbol{\nabla} \otimes \mathbf{I}_n) \tag{27}$$

where the $(nN \times nN)$ matrices of partial derivatives of $\mathbf{f}_{\mathrm{nl}}$ evaluated at $N$ time steps are defined by:

$$\frac{\partial \mathbf{f}_{\mathrm{nl}}}{\partial \mathbf{x}} = \begin{bmatrix} \mathrm{diag}\left(\frac{\partial \mathbf{f}_1}{\partial \mathbf{x}_1}\right) & \dots & \mathrm{diag}\left(\frac{\partial \mathbf{f}_1}{\partial \mathbf{x}_n}\right) \\ \vdots & \ddots & \vdots \\ \mathrm{diag}\left(\frac{\partial \mathbf{f}_n}{\partial \mathbf{x}_1}\right) & \dots & \mathrm{diag}\left(\frac{\partial \mathbf{f}_n}{\partial \mathbf{x}_n}\right) \end{bmatrix} \quad \text{and} \quad \frac{\partial \mathbf{f}_{\mathrm{nl}}}{\partial \dot{\mathbf{x}}} = \begin{bmatrix} \mathrm{diag}\left(\frac{\partial \mathbf{f}_1}{\partial \dot{\mathbf{x}}_1}\right) & \dots & \mathrm{diag}\left(\frac{\partial \mathbf{f}_1}{\partial \dot{\mathbf{x}}_n}\right) \\ \vdots & \ddots & \vdots \\ \mathrm{diag}\left(\frac{\partial \mathbf{f}_n}{\partial \dot{\mathbf{x}}_1}\right) & \dots & \mathrm{diag}\left(\frac{\partial \mathbf{f}_n}{\partial \dot{\mathbf{x}}_n}\right) \end{bmatrix}$$

(28)

and where:

$$\frac{\partial \tilde{\mathbf{f}}_{\mathrm{nl}}(\tilde{\mathbf{x}},\omega)}{\partial \omega} = \frac{\partial \tilde{\mathbf{f}}_{\mathrm{nl}}}{\partial \mathbf{f}_{\mathrm{nl}}}\frac{\partial \mathbf{f}_{\mathrm{nl}}}{\partial \omega} + \frac{\partial \tilde{\mathbf{f}}_{\mathrm{nl}}}{\partial \mathbf{f}_{\mathrm{nl}}}\frac{\partial \mathbf{f}_{\mathrm{nl}}}{\partial \dot{\mathbf{x}}}\frac{\partial \dot{\mathbf{x}}}{\partial \omega} = \mathbf{\Gamma}^{-1}\frac{\partial \mathbf{f}_{\mathrm{nl}}}{\partial \omega} + \mathbf{\Gamma}^{-1}\frac{\partial \mathbf{f}_{\mathrm{nl}}}{\partial \dot{\mathbf{x}}}\mathbf{\Gamma}(\boldsymbol{\nabla}\otimes\mathbf{I}_n)\tilde{\mathbf{x}} \tag{29}$$

### 2.4 Exact nonlinear condensation procedure

When considering large mechanical systems undergoing contact interactions, it is common practice to distinguish the linear dof $\tilde{\mathbf{x}}^{\mathrm{l}}$ from the nonlinear dof $\tilde{\mathbf{x}}^{\mathrm{nl}}$, over which structural contacts may occur. This yields a partition [36] of the system and a reorganization of its dof so that Eq. (10) may be written as:

$$\begin{bmatrix} \mathbf{Z}^{\mathrm{ll}} & \mathbf{Z}^{\mathrm{lnl}} \\ \mathbf{Z}^{\mathrm{nll}} & \mathbf{Z}^{\mathrm{nlnl}} \end{bmatrix}\begin{bmatrix} \tilde{\mathbf{x}}^{\mathrm{l}} \\ \tilde{\mathbf{x}}^{\mathrm{nl}} \end{bmatrix} + \begin{bmatrix} \tilde{\mathbf{f}}^{\mathrm{l}}_{\mathrm{nl}}(\tilde{\mathbf{x}}^{\mathrm{nl}}) \\ \tilde{\mathbf{f}}^{\mathrm{nl}}_{\mathrm{nl}}(\tilde{\mathbf{x}}^{\mathrm{nl}}) \end{bmatrix} - \begin{bmatrix} \tilde{\mathbf{f}}^{\mathrm{l}}_{\mathrm{ext}} \\ \tilde{\mathbf{f}}^{\mathrm{nl}}_{\mathrm{ext}} \end{bmatrix} = \mathbf{0} \tag{30}$$

The first line of Eq. (30) underlines that the linear dof $\tilde{\mathbf{x}}^{\mathrm{l}}$ can be expressed as a function of the nonlinear dof $\tilde{\mathbf{x}}^{\mathrm{nl}}$:

$$\tilde{\mathbf{x}}^{\mathrm{l}} = \mathbf{Z}^{\mathrm{ll}^{-1}}\left[\tilde{\mathbf{f}}^{\mathrm{l}}_{\mathrm{ext}} - \mathbf{Z}^{\mathrm{lnl}}\tilde{\mathbf{x}}^{\mathrm{nl}} - \tilde{\mathbf{f}}^{\mathrm{l}}_{\mathrm{nl}}(\tilde{\mathbf{x}}^{\mathrm{nl}})\right] \tag{31}$$

which may be used in the second line of Eq. (30) to reduce the dimension of the system to be solved to that of the nonlinear dof $\tilde{\mathbf{x}}^{\mathrm{nl}}$ only:

$$\left[\mathbf{Z}^{\mathrm{nlnl}} - \mathbf{Z}^{\mathrm{nll}}\mathbf{Z}^{\mathrm{ll}^{-1}}\mathbf{Z}^{\mathrm{lnl}}\right]\tilde{\mathbf{x}}^{\mathrm{nl}} + \left(\tilde{\mathbf{f}}^{\mathrm{nl}}_{\mathrm{nl}}(\tilde{\mathbf{x}}^{\mathrm{nl}}) - \mathbf{Z}^{\mathrm{nll}}\mathbf{Z}^{\mathrm{ll}^{-1}}\tilde{\mathbf{f}}^{\mathrm{l}}_{\mathrm{nl}}(\tilde{\mathbf{x}}^{\mathrm{nl}})\right) - \left(\tilde{\mathbf{f}}^{\mathrm{nl}}_{\mathrm{ext}} - \mathbf{Z}^{\mathrm{nll}}\mathbf{Z}^{\mathrm{ll}^{-1}}\tilde{\mathbf{f}}^{\mathrm{l}}_{\mathrm{ext}}\right) = \mathbf{0} \tag{32}$$

or, in a more compact form:

$$\mathbf{Z}_{\mathrm{red}}\tilde{\mathbf{x}}^{\mathrm{nl}} + \tilde{\mathbf{f}}_{\mathrm{nl,red}}(\tilde{\mathbf{x}}^{\mathrm{nl}}) - \tilde{\mathbf{f}}_{\mathrm{ext,red}} = \mathbf{0} \tag{33}$$

Considering Eq. (33), the gradient $\mathbf{R}_{,\omega}$ from Eq. (20) now reads:

$$\mathbf{R}_{,\omega} = \mathbf{Z}_{\mathrm{red},\omega}\tilde{\mathbf{x}}^{\mathrm{nl}} + \tilde{\mathbf{f}}_{\mathrm{nl,red},\omega} - \tilde{\mathbf{f}}_{\mathrm{ext,red},\omega} \tag{34}$$

with:

$$\mathbf{Z}_{\mathrm{red},\omega} = \mathbf{Z}^{\mathrm{nlnl}}_{,\omega} - \mathbf{Z}^{\mathrm{nll}}_{,\omega}\mathbf{Z}^{\mathrm{ll}^{-1}}\mathbf{Z}^{\mathrm{lnl}} - \mathbf{Z}^{\mathrm{nll}}\left[\mathbf{Z}^{\mathrm{ll}^{-1}}\right]_{,\omega}\mathbf{Z}^{\mathrm{lnl}} - \mathbf{Z}^{\mathrm{nll}}\mathbf{Z}^{\mathrm{ll}^{-1}}\mathbf{Z}^{\mathrm{lnl}}_{,\omega} \tag{35}$$

and:

$$\tilde{\mathbf{f}}_{\mathrm{ext,red},\omega} = \frac{\partial \tilde{\mathbf{f}}^{\mathrm{nl}}_{\mathrm{ext}}}{\partial \omega} - \mathbf{Z}^{\mathrm{nll}}_{,\omega}\mathbf{Z}^{\mathrm{ll}^{-1}}\tilde{\mathbf{f}}^{\mathrm{l}}_{\mathrm{ext}} - \mathbf{Z}^{\mathrm{nll}}\left[\mathbf{Z}^{\mathrm{ll}^{-1}}\right]_{,\omega}\tilde{\mathbf{f}}^{\mathrm{l}}_{\mathrm{ext}} - \mathbf{Z}^{\mathrm{nll}}\mathbf{Z}^{\mathrm{ll}^{-1}}\frac{\partial \tilde{\mathbf{f}}^{\mathrm{l}}_{\mathrm{ext}}}{\partial \omega} \tag{36}$$

where the derivative with respect to $\omega$ of the inverse $\mathbf{Z}^{\mathrm{ll}^{-1}}$ is obtained with the formula $[\mathbf{Z}^{\mathrm{ll}^{-1}}]_{,\omega} = -\mathbf{Z}^{\mathrm{ll}^{-1}}\mathbf{Z}^{\mathrm{ll}}_{,\omega}\mathbf{Z}^{\mathrm{ll}^{-1}}$. The expression of the reduced gradient $\tilde{\mathbf{f}}_{\mathrm{nl,red},\omega}$ is identical to the one given in Eq. (29) since it is assumed that there is no nonlinear forcing on the linear dof: $\tilde{\mathbf{f}}^{\mathrm{l}}_{\mathrm{nl}}(\tilde{\mathbf{x}}^{\mathrm{nl}}) = \mathbf{0}$.

### 2.5 Specific developments for blade-tip/casing contact treatment

The aforementioned developments are recalled for the sake of completeness. Indeed, they have already been used in the literature [37] for the management of various types of nonlinearities, including friction. When dealing with structural contacts however, it has been shown that the HBM is prone to the Gibbs phenomenon [24] and thus usually performs poorly [25].

The Gibbs phenomenon is a well-known phenomenon related to the non-uniform convergence of Fourier series for the approximation of nonsmooth functions. It translates into spurious oscillations appearing in the vicinity of

discontinuities that, in the context of the HBM, degrade the accuracy of the iterative procedure to a point that a converged solution may not be obtained. Mitigating the Gibbs phenomenon has been the focus of many research investigations. For instance, a mixed shooting-harmonic balance procedure [38] has recently been developped to this end. Discontinuous polynomial functions [39] and wavelet basis functions [26] have also been considered in conjunction or in replacement of the Fourier basis functions in order to better approximate nonsmooth functions. Other mathematical studies [40] have also shown that it is possible to successfully mitigate the Gibbs phenomenon by spectral reprojection techniques like the Gegenbauer reconstruction method. In this section, two key elements are presented to mitigate the Gibbs phenomenon:

**a regularized contact law** is first introduced in order to smoothen contact management. This regularization is applied on a bilinear penalty contact law that is later shown to provide results in very good agreement with a nonregularized reference solution strategy,

**the Lanczos filtering technique** is then considered in the frequency domain. Indeed, while the regularization of the contact law greatly increases the numerical robustness of the HBM, it does not prevent spurious oscillations on the displacements, velocities or contact forces.

### 2.5.1 Regularized contact law

In the case of unilateral contact, nonlinear contact forces $\mathbf{f}_{\mathrm{nl}}$ arise from inequality constraints defined by the Hertz-Signorini-Moreau conditions [41]. In the context of frequency methods, there are several contact treatment algorithms to compute these forces. For instance, one may mention the augmented Lagrangian [21] method and the dynamic Lagrangian frequency time [42] approach. Contact forces may also be directly computed proportionally to the computed interpenetration of the structures using a well-known penalty approach. This approach is particularly well-suited when using an AFT scheme and is used in this study.

Let $\mathbf{g}$ be the gap function which represents the signed distance between contact nodes and an obstacle:

$$\mathbf{g}(t) = \mathbf{x}(t) - \mathbf{d}(t) \tag{37}$$

where $\mathbf{d}(t)$ refers to the position of the obstacle, possibly varying with respect to time. The computation of the normal component $\hat{\mathbf{f}}_{\mathrm{nl}}$ of the nonlinear forces is done as follows:

$$\hat{\mathbf{f}}_{\mathrm{nl}}(t) = \kappa \max\left(\mathbf{0}, \mathbf{g}(t)\right) \tag{38}$$

where $\kappa \in \mathbb{R}_+$ is the so-called penalty coefficient and the max function provides a pairwise maximum of two vectors. The penalty coefficient should be large enough to prevent significant residual penetrations but should also remain below a certain threshold over which numerical instabilities may arise due to ill-conditioned matrices in Eq. (10).

In order to further enhance the robustness of the proposed methodology, the penalty contact law is smoothened [29]:

$$\hat{f}_{\mathrm{nl},j}(t) = \kappa \frac{g_j(t)}{2} + \sqrt{\left(\kappa \frac{g_j(t)}{2}\right)^2 + \gamma^2} \tag{39}$$

where $\gamma \in \mathbb{R}_+$ is an additional penalty parameter allowing adjustable smoothing, and $\hat{f}_{\mathrm{nl},j}$ and $g_j$ respectively refer to coordinates of vectors $\hat{\mathbf{f}}_{\mathrm{nl}}$ and $\mathbf{g}$. It should be underlined that Eqs. (38) and (39) are equivalent when $\gamma = 0$. The two penalty laws (38) and (39) are illustrated in Fig. 4.

### 2.5.2 Lanczos filtering technique

The regularization of the contact law has a strong influence on improving the numerical robustness of the solver but only moderately reduces the Gibbs phenomenon. In order to further mitigate the effects of the Gibbs phenomenon, filtering techniques are employed. One manifestation of the Gibbs phenomenon is that Fourier coefficients decay too slowly. For that reason, filtering techniques aim at altering these coefficients in order to make them decay faster. Classical filters include the raised cosine filter, family of exponential filters, Fejér averaging and the second order Lanczos filter (also known as $\sigma$-approximation or Lanczos $\sigma$-averaging) [24, 40]. In this paper, the Lanczos

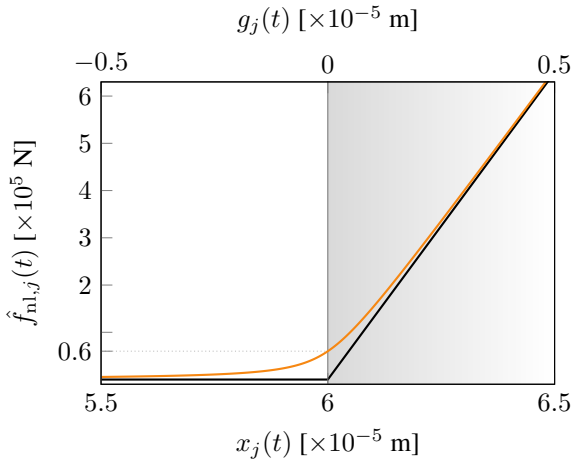


**Figure 4** – Comparison of the bilinear penalty law (38) (——) and its smoothened counterpart (39) (——) for $\kappa = 1.3 \cdot 10^{11}$ N·m$^{-1}$ and $\gamma = 6 \cdot 10^4$ N for a rigid obstacle (□) at fixed distance $d_j(t) = 6 \cdot 10^{-5}$ m.

filtering technique is used, it is found to provide the best compromise between spurious oscillations mitigation and an accurate approximation of the original waveform in the vicinity of discontinuous areas.

The application of a Lanczos filter on nonlinear forces $\mathbf{f}_{\mathrm{nl}}$ introduced in Eq. (2) reads:

$$\mathbf{f}_{\mathrm{nl}}(\mathbf{x}, \dot{\mathbf{x}}) \simeq \frac{1}{2}\mathbf{a}_0^{\mathrm{nl}} + \sum_{j=1}^{H} \underbrace{\mathrm{sinc}\left(\mathcal{X}_j\right)^m}_{\sigma_j} \left[\mathbf{a}_j^{\mathrm{nl}} \cos\left(j\omega t\right) + \mathbf{b}_j^{\mathrm{nl}} \sin\left(j\omega t\right)\right] \tag{40}$$

where $\mathrm{sinc}\left(x\right) = \sin\left(\pi x\right)/\pi x$ is the normalized cardinal sine function used to define Lanczos factors $\sigma_j$ and $\mathcal{X}_j$ controls the amount of filtering for each harmonic of the truncated Fourier series, it is defined by:

$$\mathcal{X}_j = \frac{\rho_j}{H+1} \text{ for } j \in [\![0..H]\!] \tag{41}$$

where numerator parameter $\rho_j$ is built around a cut-off harmonic $C_H$ that allows the control of the start of the filtering window:

$$\rho_j = \begin{cases} 0 & \text{for } j < C_H \\ j & \text{for } C_H \leq j \leq H \end{cases} \tag{42}$$

The parameter $m$ controls the smoothing intensity as it allows to carry out $m$-repeated averagings [24, 43], as depicted in Fig. 5 (for $C_H = 1$). One may note that when $m = 0$, all Lanczos factors become unitary, therefore Fourier coefficients are not altered and the original operator is retrieved. Moreover, variable $\mathcal{X}_j$ of the filtering function defined in relation (41) always stays inferior to one so that even highest harmonic contribution is not totally filtered out. In order to apply Lanczos filtering in the context of HBM, the forward DFT operator (26) is modified by balancing each harmonic $j$ with the corresponding $\sigma_j$ factor.

Preliminary investigations on a single dof oscillator undergoing unilateral contact conditions with a moving rigid obstacle, not detailed here for the sake of brevity, underlined that filtering techniques significantly improve the convergence of the HBM. Even when considering a regularization of the contact law, the HBM would often not converge without any filtering. While filtering may yield both phase and amplitude distortions, thus potentially degrading the calculation accuracy, it was found to be highly beneficial in terms of mitigating the Gibbs phenomenon while preserving very accurate results for all the investigated systems in this study.

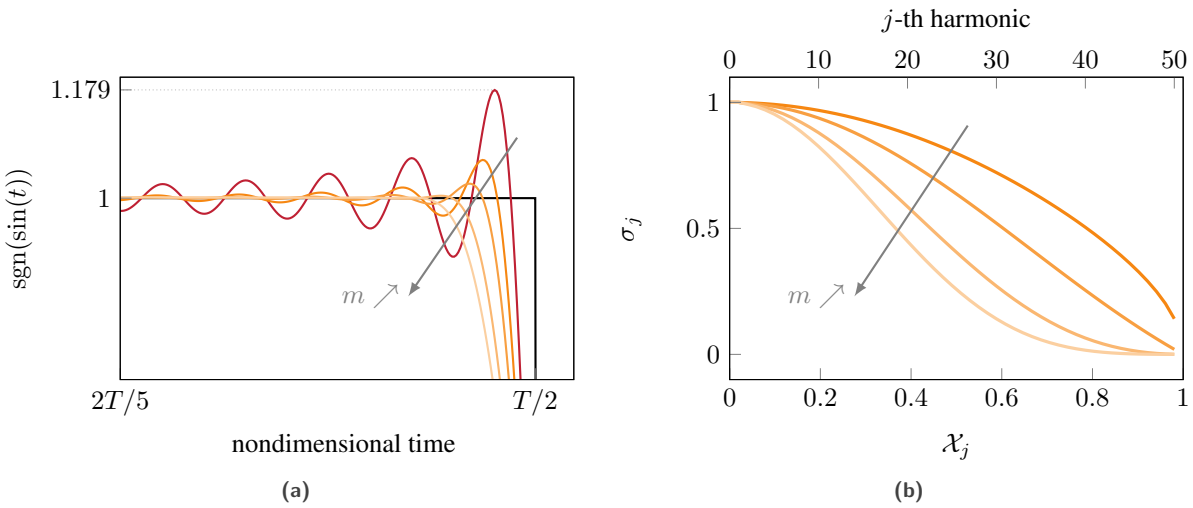


**Figure 5** – Illustration of the Lanczos filtering technique: (a) Gibbs phenomenon for the approximation of a $T$-periodic square wave (——) by a Fourier series truncated at $H = 50$ (——) and with Lanczos filter for different values of $m$, and (b) Lanczos factors obtained with different $m$. Legends: $m = 0.5$ (——), $m = 1$ (——), $m = 2$ (——) and $m = 3$ (——).

## 3 Validation

An academic test case is here employed in order to validate the proposed methodology's numerical robustness as well as its efficiency to mitigate the Gibbs phenomenon. This academic test case is also used to assess the accuracy of the contact treatment procedure with respect to a reference solution strategy relying on numerical time integration and a Lagrange multiplier-based approach for contact treatment.

For the sake of brevity, in the remainder, the expression *Regularized HBM* (R-HBM) is used to refer to the proposed methodology with the regularized contact law only. Similarly, the expression *Regularized-Lanczos HBM* (RL-HBM) is used to refer to the proposed methodology with the regularized contact law and the Lanczos filtering procedure.

### 3.1 Academic test case

The considered academic test case is that of a flexible rod impacting a rigid obstacle, as depicted in Fig. 6. The

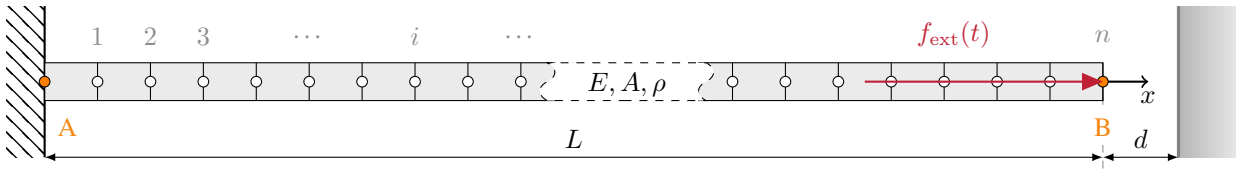


**Figure 6** – Finite-element clamped-free rod model and obstacle (▭).

mechanical properties of the rod and the excitation parameters are chosen so as to maximize the amplitude of the nonlinear resonance and thus increase the numerical severity of the contact configuration. The rod's length is $L = 1$ m, its Young's modulus is $E = 21$ GPa and its density is $\rho = 7500$ kg·m$^{-3}$. The left extremity A is clamped, while the other one is subject to an external harmonic forcing $f_{\text{ext}}(t) = F_0 \cos(\omega t)$ with $F_0 = 25000$ N. At rest, the right extremity B is located at $\mathbf{d}(t) = d = 6 \cdot 10^{-5}$ m of a rigid wall.

The rod's finite element mesh is made of $n = 100$ identical elements of length $l = L/n$ and section area

$A = 0.05$ m$^2$. For the sake of completeness, elementary finite element matrices are given below:

$$\mathbf{M}_{\mathrm{e}} = \frac{\rho A l}{6}\begin{bmatrix} 2 & 1 \\ 1 & 2 \end{bmatrix} \quad \text{et} \quad \mathbf{K}_{\mathrm{e}} = \frac{EA}{l}\begin{bmatrix} 1 & -1 \\ -1 & 1 \end{bmatrix} \tag{43}$$

Finally, structural damping is accounted for using one identical modal damping coefficient $\xi = 7.5 \cdot 10^{-3}$ for all free-vibration modes.

### 3.2 Reference solution strategy and calibration of contact stiffness

As mentioned above, all results presented in the article are compared to a reference numerical strategy [44] relying on numerical time integration (TI) and a Lagrange multiplier-based approach [17]. However, for this first validation, in order to validate the proposed methodology without introducing possible numerical artifacts related to the contact treatment algorithm, the TI reference strategy is combined with a non regularized penalty approach for contact management. One drawback of using of penalty laws for contact management is the dependence of the results to the stiffness coefficient $\kappa$. Low values of $\kappa$ yield significant interpenetrations of the impacting structures while too high values of this parameter may lead to numerical instability of the solver. For that reason, the TI reference strategy is first employed to define a suitable contact stiffness for the academic test case.

Contact simulations of the academic test case are carried out with the TI reference strategy with an excitation frequency corresponding to the first eigenfrequency of the linear system: $\omega_1 = 2628$ rad·s$^{-1}$. Once a steady state has been reached, results obtained with Lagrange multipliers and penalty laws are superimposed in Fig. 7. Results obtained for the lowest values of $\kappa$ feature significant interpenetrations but it can be seen in Fig. 7 that

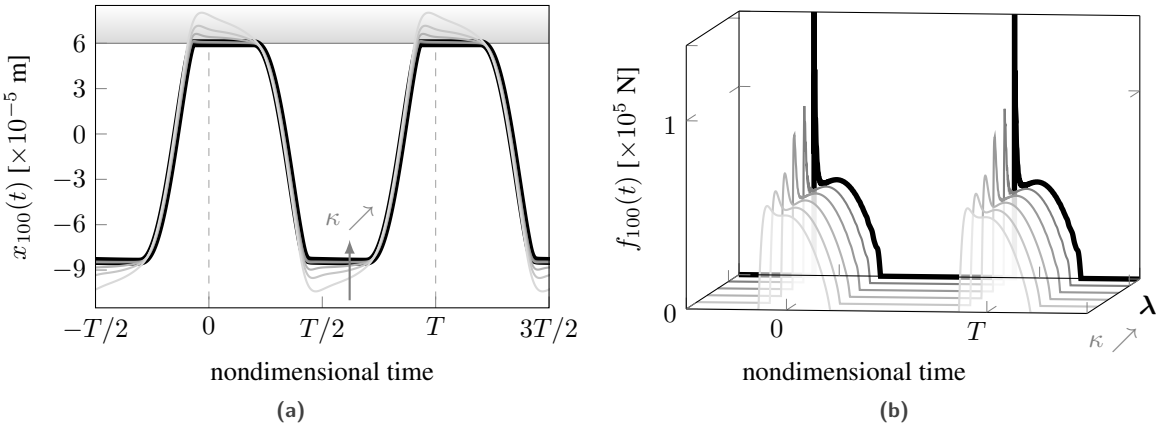


**Figure 7** – Steady states obtained with the TI reference strategy for $\omega_1 = 2628$ rad·s$^{-1}$, with the penalty method for $\kappa = \{3.3 \cdot 10^9,\ 6.3 \cdot 10^9,\ 1.3 \cdot 10^{10},\ 6.3 \cdot 10^{10},\ 1.3 \cdot 10^{11}\}$ N·m$^{-1}$ (——) and Lagrange multipliers $\lambda$ (——): (a) displacements and (b) normal contact forces.

increasing $\kappa$ leads to results almost perfectly superimposed with those obtained using a Lagrange multiplier-based approach for contact treatment. In terms of contact forces, one may note that the agreement between the Lagrange multiplier-based approach and the penalty method is overall very good, even for low stiffness coefficients. Highest stiffness coefficients tend to better capture the contact force impulse at contact initiation. The discrepancy observed between the impulse predicted with Lagrange multipliers and penalty method is related to well-known numerical artifacts inherent to the Lagrange multipliers approach and thus should not be accounted for in this comparison.

The stiffness coefficent $\kappa = 1.3 \cdot 10^{11}$ N·m$^{-1}$ yields the best compromise between accuracy of the solution and limited interpenetrations. The transient time response obtained for this stiffness coefficient is superimposed with the transient time response obtained with Lagrange multipliers in Fig. 8 where it can be seen that results are also almost a perfect match. Based on these observations, all computations run in the following of this section with the proposed methodology feature a stiffness coefficient $\kappa = 1.3 \cdot 10^{11}$ N·m$^{-1}$.

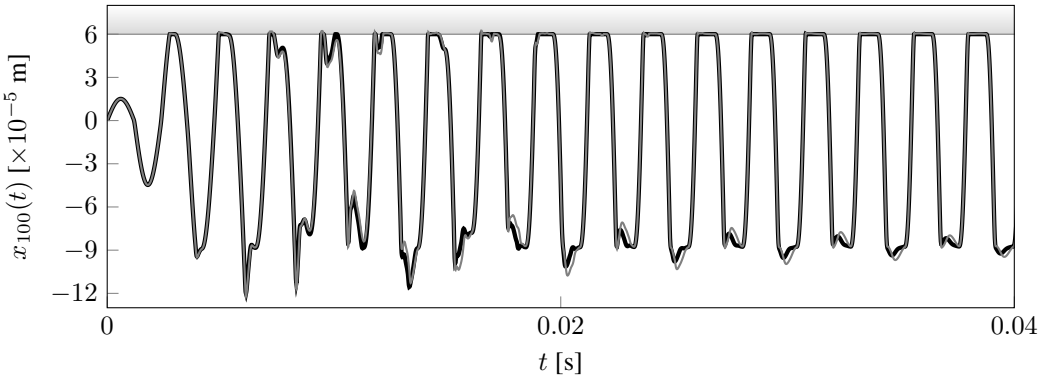


**Figure 8** – Transient time responses obtained with Lagrange multipliers (——) and penalty method for $\kappa = 1.3 \cdot 10^{11}$ N·m$^{-1}$ (——).

### 3.3 Full finite element model

#### *3.3.1 Nonlinear frequency response curves*

The NFRC obtained in the vicinity of $\omega_1$ with the TI reference strategy, R-HBM and RL-HBM are plotted in Fig. 9. A thorough convergence analysis, not presented here for the sake of brevity, led to the definition of HBM numerical parameters as follows: $H = 30$, $N = 1024$ and $\gamma = 6 \cdot 10^4$ N. A sequential continuation procedure was added to the TI reference strategy to carry out upward and downward frequency sweeps. This sequential continuation consists is using as initial conditions of the time integration procedure the converged solution obtained at the previous iteration on the angular frequency $\omega$. Upward and downward frequency sweeps reveal jump phenomena respectively located at $\omega = 3355$ rad·s$^{-1}$ and $\omega = 2993$ rad·s$^{-1}$. In addition, around $\omega = 2800$ rad·s$^{-1}$, the amplitudes predicted by the TI reference strategy are not steady.

Overall, the NFRC obtained with R-HBM (——) and RL-HBM (——) are almost perfectly superimposed with the solutions obtained with the TI reference strategy. The only noticeable difference is found in the vicinity of the nonlinear resonance where it is found that the proposed methodology tends to slightly overestimate the maximum amplitude of the displacements, see area ③ in Fig. 9. A Lanczos filter with unitary characteristics was found to offer

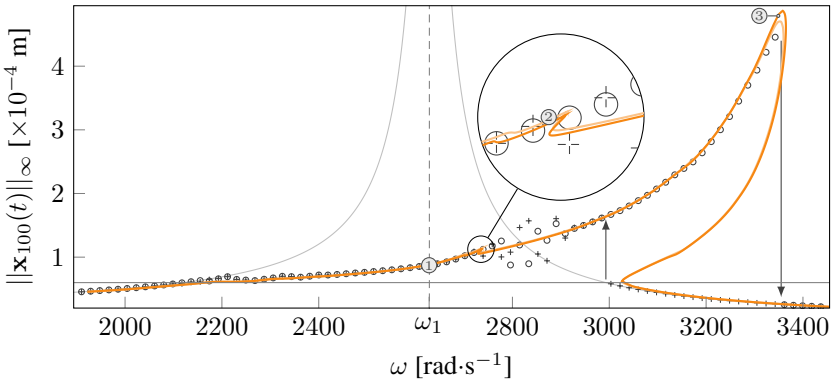


**Figure 9** – NRFC obtained with the TI reference strategy (upward (○) and downward (+) frequency sweeps), by R-HBM (——) and RL-HBM (——). Linear FRF (——) and contact threshold (——).

a good trade-off between accuracy of the solutions, reduction of oscillations and convergence of the algorithm.

### 3.3.2 Influence of contact regularization and filtering

In order to better understand the influence of both contact regularization and the Lanczos filtering technique on the obtained results, the emphasis is here made on the solution obtained at the linear resonance $\omega_1$, marked as area ① in Fig. 9. This point is of special interest since the standard HBM solver without regularization and filtering is able to provide a solution in this area but fails to converge as soon as $\omega \geq 1.02\,\omega_1$. It is thus possible, at this point, to compare the solutions provided by TI, HBM, R-HBM and RL-HBM.

Firstly, the frequency spectra of solutions obtained with the TI reference strategy, R-HBM and RL-HBM are depicted in Fig. 10. A semi-logarithmic scale is used to better visualize the differences between the three spectra. The limit in terms of number of harmonics ($H = 30$) does not apply to the TI reference solution, harmonics 31 and higher can thus be depicted in Fig. 10. Associated amplitudes are about three to four orders of magnitude smaller than the maximum amplitude of the fundamental harmonics which justifies *a posteriori* the selected value for $H$. The influence of the Lanczos filtering technique is evidenced for harmonics 15 and higher with a significant drop in the amplitudes associated to these harmonics for the RL-HBM solution.

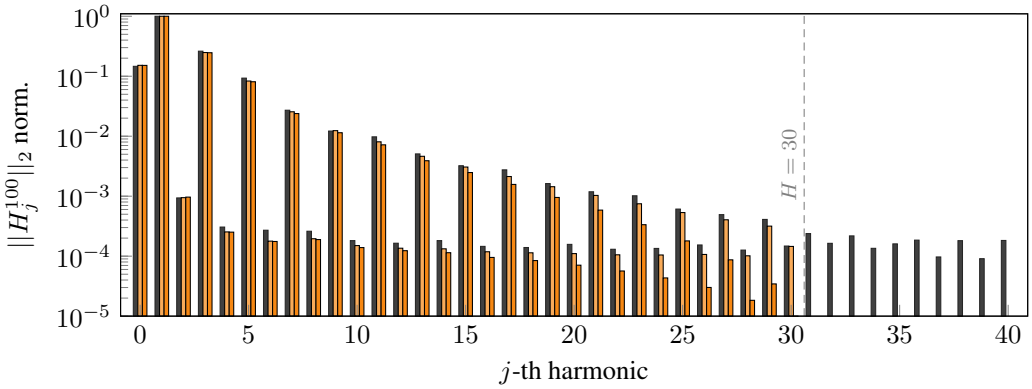


**Figure 10** – Frequency spectra of solutions obtained at $\omega_1 = 2628$ rad·s$^{-1}$ ① with the TI reference strategy (■), R-HBM (■) and RL-HBM (■).

The comparison between each of these spectra with respect to the frequency spectrum of the solution obtained with standard HBM is given in Fig. 11. Interestingly, TI, R-HBM and RL-HBM all feature significantly lower amplitudes for high harmonics (15 to 30). For lower harmonics, it should be underlined that the most significant differences between the TI reference solution and the standard HBM solution are found for even harmonics which amplitudes are several orders of magnitude lower than those of odd harmonics, see Fig. 10: for that reason, differences reaching 15 to 50 % for harmonics 4, 6, 8 and 12 are not deemed meaningful. Without exception, it is found that there is a gradation in the reduction of amplitudes of odd harmonics from the TI solution to the regularized HBM solution and from the regularized HBM to the regularized-Lanczos HBM solution. This reduction is key in the mitigation of spurious oscillations that can be seen in the time domain.

### 3.3.3 Time domain comparison

Because of the intricated dynamic behavior of the system in area ②, it is considered as a good test area for assessing the accuracy of the proposed methodology. The linear and nonlinear resonance areas—① and ③ in Fig. 9—are also considered for this time-domain comparison.

Displacements of the rod's extremity and predicted contact forces are shown for each configuration in Fig. 12. There is a very good agreement between each TI reference solution and the related R-HBM and RL-HBM solutions. A close inspection of contact forces at the beginning of a contact phase underlines that the R-HBM solutions feature significant oscillations. This confirms that contact regularization alone cannot prevent spurious oscillations. However, these oscillations are almost completely vanished for the RL-HBM solutions thus confirming the relevance of the Lanczos filtering technique.

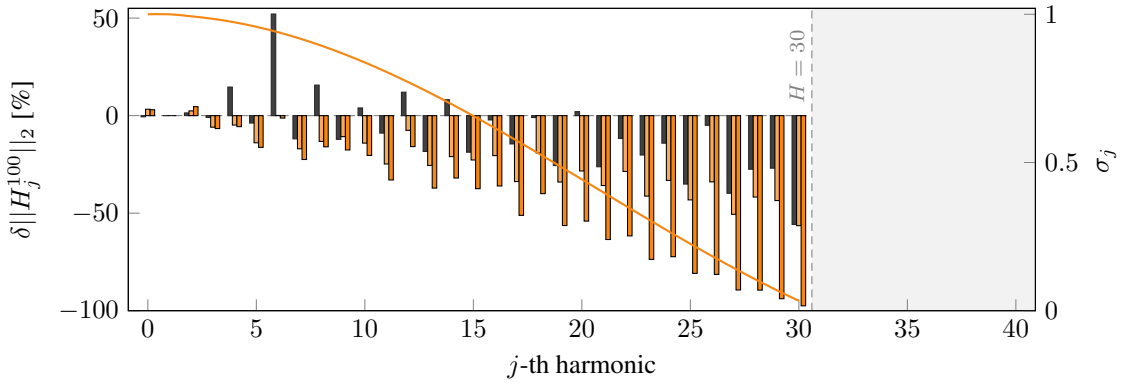


**Figure 11** – Differences between the frequency spectra of the solutions obtained at $\omega_1 = 2628$ rad·s$^{-1}$ ① by the TI reference strategy (■), R-HBM (■) and RL-HBM (■) with respect to the standard HBM. Lanczos filter profile (—).

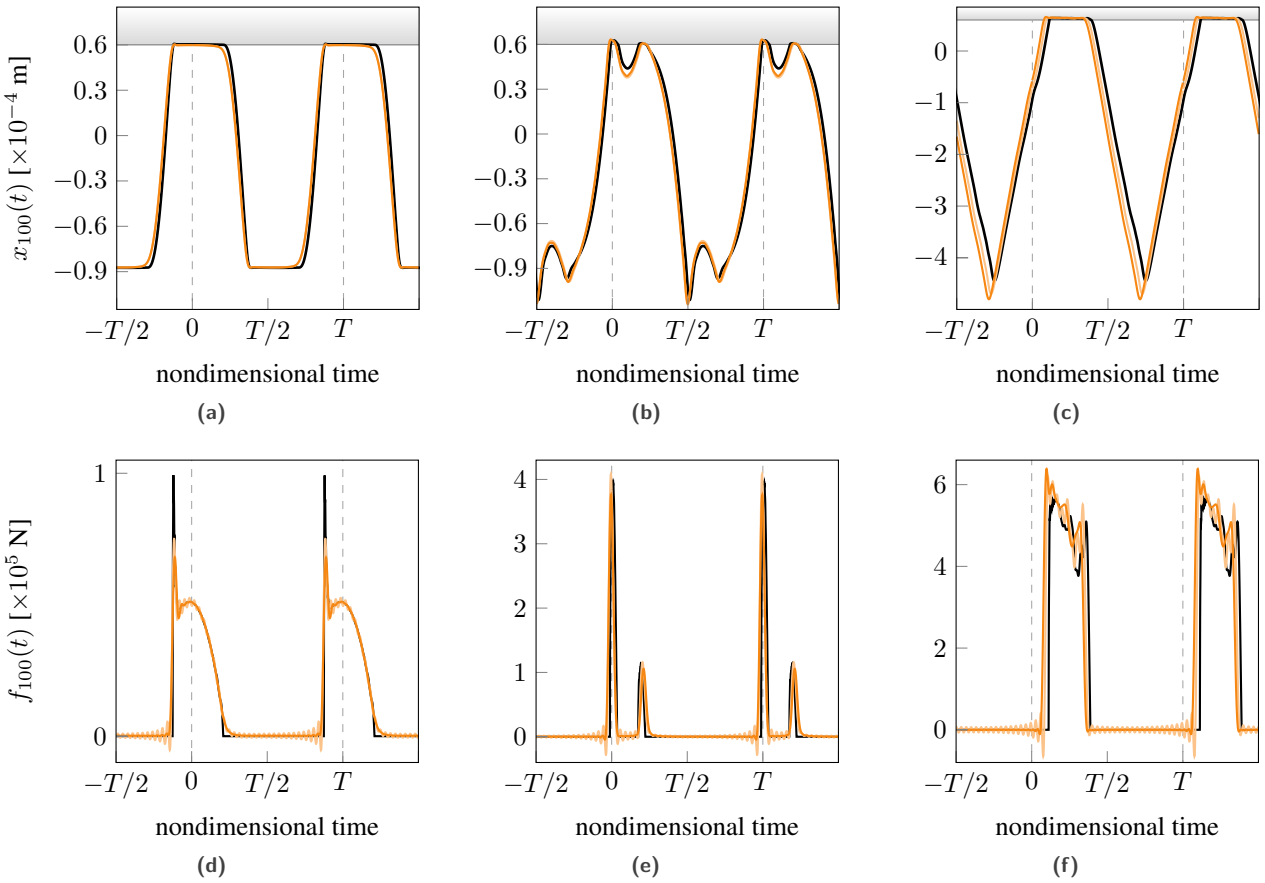


**Figure 12** – Solutions obtained with the TI reference strategy (—), R-HBM (—) and RL-HBM (—). Displacements and contact forces for areas: (a) (d) ①, (b) (e) ②, and (c) (f) ③.

### 3.4 Reduced-order model

The rod of interest yields a finite element model with a fairly small number of dof, it may thus be used directly in the proposed methodology. However, for industrial applications such as the ones targeted in this article, large finite element models featuring hundreds of thousands dof are the norm. For such models, the proposed methodology cannot be applied directly. A common strategy to reduce the dimension of the system without degrading its physical relevance is to use model reduction, such as component mode synthesis techniques.

In particular, it has been shown that the Craig-Bampton method [45] is well-suited for problems with localized nonlinearities such as in the case of contact [46]. Its numerical robustness is a major asset for nonlinear dynamic simulations. This method is considered in this subsection in conjuction with the proposed methodology. A Craig-Bampton reduced-order model is built by projecting the structural matrices in a suitable subspace spanned by a set of constraint modes (whose number is equal to the number of dof in the system's nonlinear interface) and fixed modes (whose number, denoted $\eta$, is the reduction parameter controlling the accuracy of the model). More details about the Craig-Bampton method may be found in [45].

For the sake of brevity, results obtained with the RL-HBM methodology combined with model reduction are only shown in the time domain, considering the same TI reference solutions—with the full finite element model—as in section 3.3.3.

#### *3.4.1 Displacements and forces*

Displacements of the rod's extremity and predicted contact forces are shown for each configuration in Fig. 13. Several values of the reduction parameter $\eta$ are considered, ranging from 5 to 20. Displacements depicted in Figs. 13a, 13b and 13c reveal that for such values of $\eta$, there is practically no visible differences between the solutions: only minor oscillations are noticeable during contact phases in Fig. 13a for $\eta = 5$. These oscillations translate into strong fluctuations of the contact forces, see Fig. 13d, that disappear promptly as $\eta$ increases. In the end, for the investigated rod system, converged results are obtained for $\eta \geq 15$ and it is evidenced that modal reduction does not have any negative influence on the proposed methodology.

#### *3.4.2 Velocities*

As a final step in the validation of the presented methodology, it is here proposed to have a look at the velocity fields. This quantity is of great interest as contacts unavoidably yield discontinuous velocities with respect to time. When approximated with Fourier series, it is thus highly sensitive to the Gibbs phenomenon and usually require a higher number of harmonics to reach convergence in comparison to the one needed for displacements. The velocity of the rod's extremity for areas ①, ② and ③ of Fig. 12 are plotted in Fig. 14, using $\eta = 15$ as a reduction parameter. Overall, there is an excellent agreement between the TI reference solutions—obtained with the full finite element model—and the RL-HBM solutions with a reduction parameter $\eta = 15$.

### 3.5 Partial conclusion

Results presented in the previous subsections highlight the suitability of the RL-HBM methodology for the analysis of a numerically sensitive contact problem between a rod and a rigid obstacle. In particular, it is shown that the Lanczos filtering technique plays a key role in mitigating spurious oscillations related to the Gibbs phenomenon. Beside of the suitability of the proposed methodology, the very good agreement of the obtained results with respect to the TI reference strategy also provides insight on the sensitivity of contact simulations with respect to the contact management algorithm. Indeed, while penalty based approaches may often be described as less accurate than Lagrange multiplier-based algorithms, notably due to the fact that they inherently allow residual penetrations, it is here evidenced that they provide results in very good agreement with the TI solutions that rely on a Lagrange-multiplier based algorithm. The obvious limitation of the rod test case lies in the fact that it features a single nonlinear dof. The industrial application presented in the remainder goes beyond this limitation and allows to account for more realistic contact interfaces and friction.

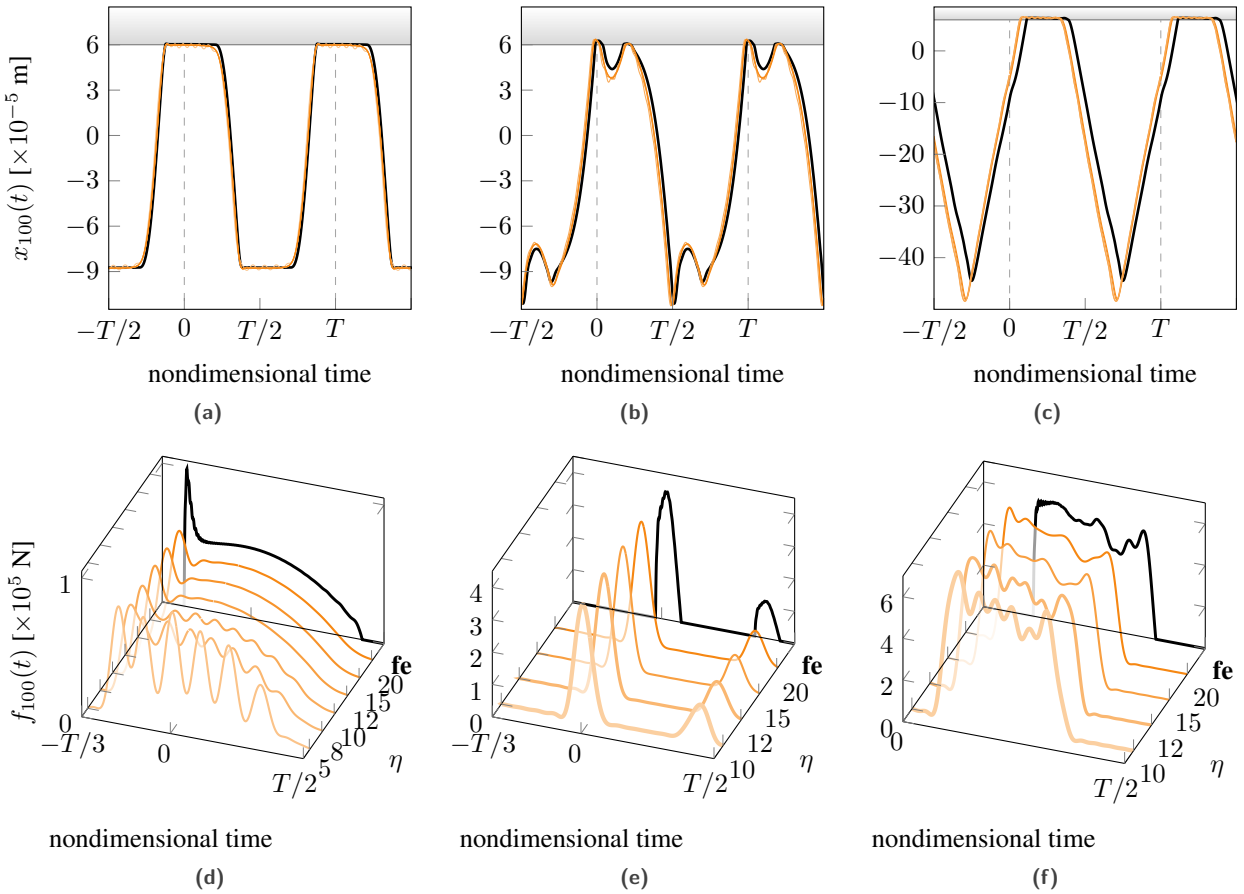


**Figure 13** – Solutions obtained by RL-HBM (——) for various reduction parameter $\eta$ and TI reference strategy (——) on full finite element model (**fe**). Displacements and contact forces for areas: (a) (d) ①, (b) (e) ②, and (c) (f) ③.

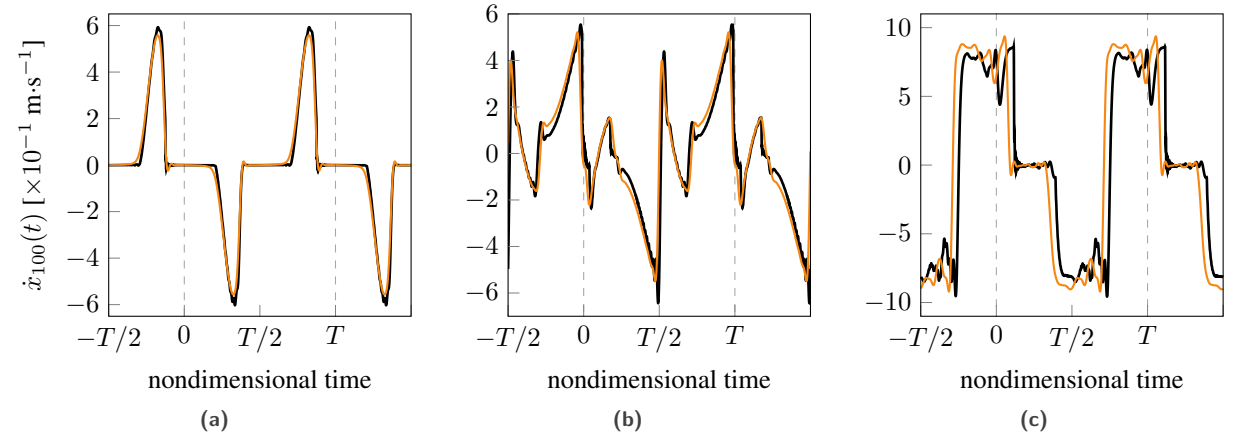


**Figure 14** – Velocities obtained by RL-HBM (——) and TI reference strategy (——) for areas: (a) ①, (b) ②, and (c) ③.

## 4 Industrial application

Rotor 37 is a 36-blade transonic axial compressor stage, see Fig. 15a. Designed at NASA's Lewis research center in the late 1970s [47] as part of aerodynamics research, NASA rotor 37's experimental results and geometry have been widely used in the field of computational fluid dynamics. It notably served as a benchmark to assess the performance of numerical solvers throughout the 1990s. Rotor 37 is today a standard test case in the field of fluid mechanics. More recently, a single blade has been used to develop a reference configuration for the analysis of blade-tip/casing contact interactions [48]. It is also used in this paper as a case study by means of the proposed RL-HBM.

### 4.1 Blade modelling

Rotor 37 is made of a nickel-based alloy: maraging steel grade 200. More precisely, the mechanical properties of a 18-Ni 200-maraging alloy [48] are considered for the numerical simulations with a Young's modulus $E = 180$ GPa, a density $\rho = 8000$ kg·m$^{-3}$, a Poisson's ratio $\nu = 0.3$ and a yield stress $\sigma_Y = 1.38$ GPa.

The 3D finite element model of the blade comprises 1800 quadratic hexahedral elements with 5745 nodes, it is depicted in Fig 15b. A reduced-order model, built with the Craig-Bampton approach, is obtained considering a reduction parameter $\eta = 10$. The contact interface, shown in Fig. 15b, spreads all along the blade-tip and contains the 3 dof of $n_b = 8$ boundary nodes. The reduced model contains 24 nonlinear dof along with 10 modal dof thus yielding a total of 34 dof. Convergence of the blade eigenfrequencies for the first free vibration modes with respect to the mesh size as well as to the reduction parameter $\eta$ was checked but is not detailed here for the sake of brevity. The blade's structural damping is represented by modal damping, using a coefficient $\xi = 1 \cdot 10^{-3}$ for the first bending and torsional modes, and $\xi = 5 \cdot 10^{-3}$ for all other modes. Centrifugal effects are not taken into account in this study.

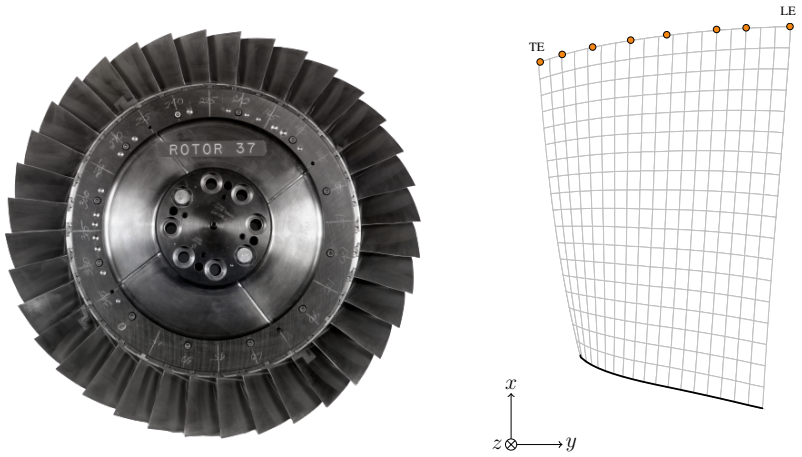


(a) (b)

**Figure 15** – NASA rotor 37: (a) full stage as shown in [49] and (b) finite element mesh of one blade.

### 4.2 Contact scenario

As is often the case for the simulation of blade-tip/casing structural contact simulations, aerodynamic forcing is here neglected, therefore $\mathbf{f}_{\text{ext}}(\omega, t) = \mathbf{0}$. This assumption is consistent with the fact that most experimental observations related to blade-tip/casing interactions were made within vacuum chambers [12]. Experimental observations also repeatedly underlined that the vibration amplitudes of the surrounding casing are negligible, which justifies that it may be considered as a perfectly rigid obstacle. Within an aircraft engine, blade-tip/casing contact may be initiated by a sudden acceleration of the blade—thus resulting in the application of a significant centrifugal load and a significant radial displacement of the blade-tip—or a progressive deformation of the surrounding casing due, for

instance, to the application of a thermal loading. In any case, accounting for a non perfectly circular casing contact surface and typical mounting points of the casing in aircraft engines often led researchers to consider a deformed casing, usually ovalized with two privileged contact areas.

In the following, the casing is represented by a perfectly rigid mathematical profile. This profile is assumed to be distorted in such a way that there are two symmetrical privileged contact areas along the casing circumference. Because of this distortion, contacts occur at any angular speed.

### 4.3 Casing distortion

The ovalized casing ($n_l = 2$ lobes are considered), in the context of the proposed methodology, translates into a time-dependent distance function in Eq. (37). In agreement with the notations introduced in Eq. (22), it is denoted:

$$\mathbf{d} = [\mathbf{d}_1, \dots, \mathbf{d}_{n_b}]^\top = [d_{1,0}, \dots, d_{1,N-1}, \dots, d_{n_b,0}, \dots, d_{n_b,N-1}]^\top \tag{44}$$

where relative distance functions components for each of the 8 boundary nodes and at each nondimensional time step $\tau_i = \omega t_i$ are evaluated as follows:

$$d_j(\tau_i) = d_{j,i} = c_j - (c_j + p_j) \exp\left[ - \left( \frac{(\tau_i + \theta_j) \pmod{2\pi/n_l} - \pi/n_l}{w_l} \right)^2 \right] \text{ for } j \in [\![1..n_b]\!],\ i \in [\![0..N-1]\!] \tag{45}$$

where $w_l$ is a weight parameter that defines the angular width of the contact areas along the casing circumference, $\theta_j$ is the angular shift of the $j$-th boundary node with respect to the reference position of the blade, $c_j$ is the operating clearance and $p_j$ defines the penetration of the casing profile with respect to the circle defined by the radial position of the $j$-th boundary node when the blade does not vibrate. The following values are considered in the remainder: $w_l = 0.15$, and for all contact nodes, $c_j = 5 \cdot 10^{-4}$ m and $p_j = 1.25 \cdot 10^{-4}$ m. One lobe of the casing is illustrated in Fig. 16.

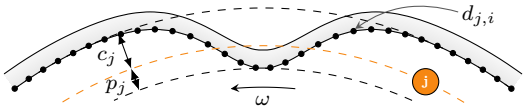


**Figure 16** – Distorted casing (▭) of the $j$-th boundary node.

### 4.4 Contact and friction management

Considering the same notations as in Eq. (22), normal contact forces in the radial direction $\mathbf{f}_{3j-2,i}$ are computed with the regularized penalty law given in Eq. (39) with $\kappa = 1 \cdot 10^9$ N·m$^{-1}$ and $\gamma = 6 \cdot 10^2$ N. In the tangential and axial directions, dry friction forces are accounted with the Coulomb law, the friction coefficient is denoted $\mu$. Permanent sliding is assumed at all time because of the very high relative speeds between the blade-tip and the casing contact surface. Circumferential $\mathbf{f}_{3j-1,i}$ and axial $\mathbf{f}_{3j,i}$ friction forces components may thus be respectively written as:

$$f_{3j-1,i} = \mu \frac{\dot{x}_{3j-1,i} + \rho_j \omega}{\sqrt{\left(\dot{x}_{3j-1,i} + \rho_j \omega\right)^2 + \dot{x}_{3j,i}^2}} f_{3j-2,i} \text{ for } j \in [\![1..n_b]\!],\ i \in [\![0..N-1]\!] \tag{46}$$

and:

$$f_{3j,i} = \mu \frac{\dot{x}_{3j,i}}{\sqrt{\left(\dot{x}_{3j-1,i} + \rho_j \omega\right)^2 + \dot{x}_{3j,i}^2}} f_{3j-2,i} \text{ for } j \in [\![1..n_b]\!],\ i \in [\![0..N-1]\!] \tag{47}$$

where $\rho_j$ is the radial position of the $j$-th boundary node. The friction coefficient is set to $\mu = 0.15$.

### 4.5 Results

The considered contact configuration with the NASA rotor 37 blade is actually the one that was used to plot the interaction maps depicted in Fig 1 using the TI reference strategy (one simulation was run every 0.5 rad·s$^{-1}$ with a time step $h = 2.5 \cdot 10^{-7}$ s and over 200 blade revolutions). These results are thus used in this section as a reference point to which results obtained with the proposed methodology are thoroughly compared. The fact that the TI reference strategy was specifically validated by confrontation to experimental results in the context of blade-tip/casing contact interactions [5, 13, 6] motivates its choice as a reference point. From an implementation standpoint, it should be underlined that the TI reference strategy thus fundamentally differs from the RL-HBM both in terms of solution paradigm (numerical time integration/frequency method) and contact treatment (Lagrange multipliers/ regularized penalty method). All RL-HBM computations are carried out with $H = 40$ and $N = 1024$. These values have been obtained from a convergence study that is detailed in the following subsection.

#### *4.5.1 Numerical convergence analysis*

The convergence of the proposed methodology is here assessed with respect to two key numerical parameters: the number $H$ of retained harmonics and the number $N$ of time samples in the time domain.

**number of retained harmonics:** $H$ The NFRC of both the leading and trailing edges radial displacements are plotted in Fig. 17 using $N = 1024$ time samples and a number of retained harmonics ranging from $H = 5$ to $H = 80$. It is noticeable that lower values of $H$ yield degraded results, with a significant overestimation

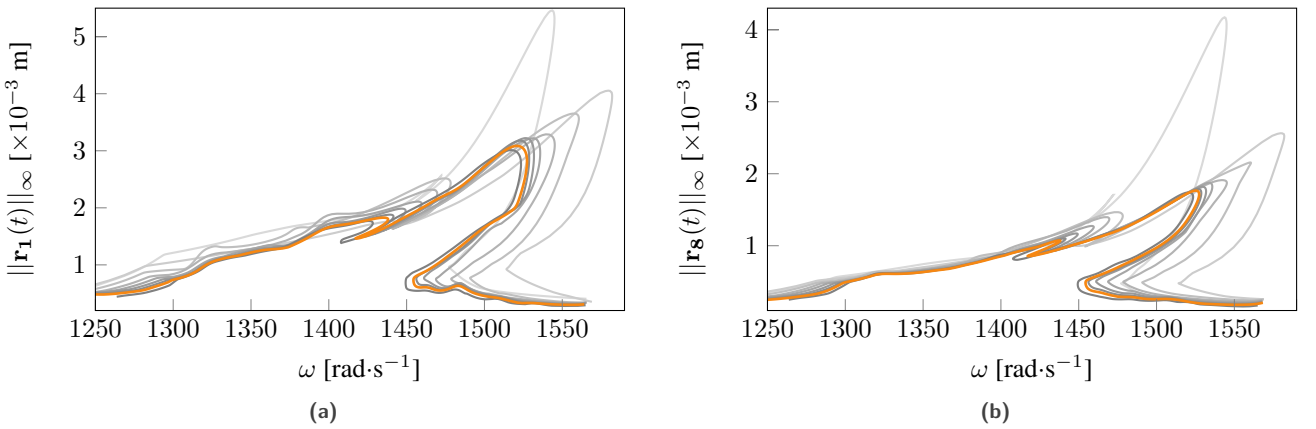


**Figure 17** – NFRC computed with RL-HBM ($N = 1024$) for $H = \{5$ (——), 10 (——), 15 (——), 20 (——), 25 (——), 30 (——), 35 (——), 40 (——), 80 (——)$\}$ at (a) LE and (b) TE.

of both the frequency and the amplitude at the nonlinear resonance. As $H$ increases, the computed NFRC become closer and closer thus underlining the asymptotical convergence of RL-HBM results. Only very minor differences are noticeable between the NFRC obtained for $H = 40$ and $H = 80$ so that results are assumed to be converged for $H = 40$. This value is used for all RL-HBM calculations in the following.

**number of time samples:** $N$ This parameter is critical to control aliasing errors. The latter may lead to divergence, turnaround of the continuation procedure, or numerical oscillations of the NFRC [29]. NFRC computed with RL-HBM for $H = 40$ and a number of time samples varying between $N = 128$ and $N = 4096$ are depicted in Fig. 18. A magnification over the most numerically sensitive areas—turning point around $\omega = 1430$ rad·s$^{-1}$ and nonlinear resonance—is provided in Figs. 18c and 18d to better visualize the influence of $N$. Beside of the lowest value $N = 128$ for which the NFRC features visible spurious oscillations, the value of $N$ has low to no impact on the shape of the NFRC. However, increasing $N$ very significantly decreases the required number of solution points over the NFRC which indicates an overall enhanced efficiency of the numerical procedure. Noticeably, the number of required solution points becomes stable for $N \geq 1024$. It is shown in Fig. 18b that the use of filtering techniques reduces—by about 10 % on average—the required

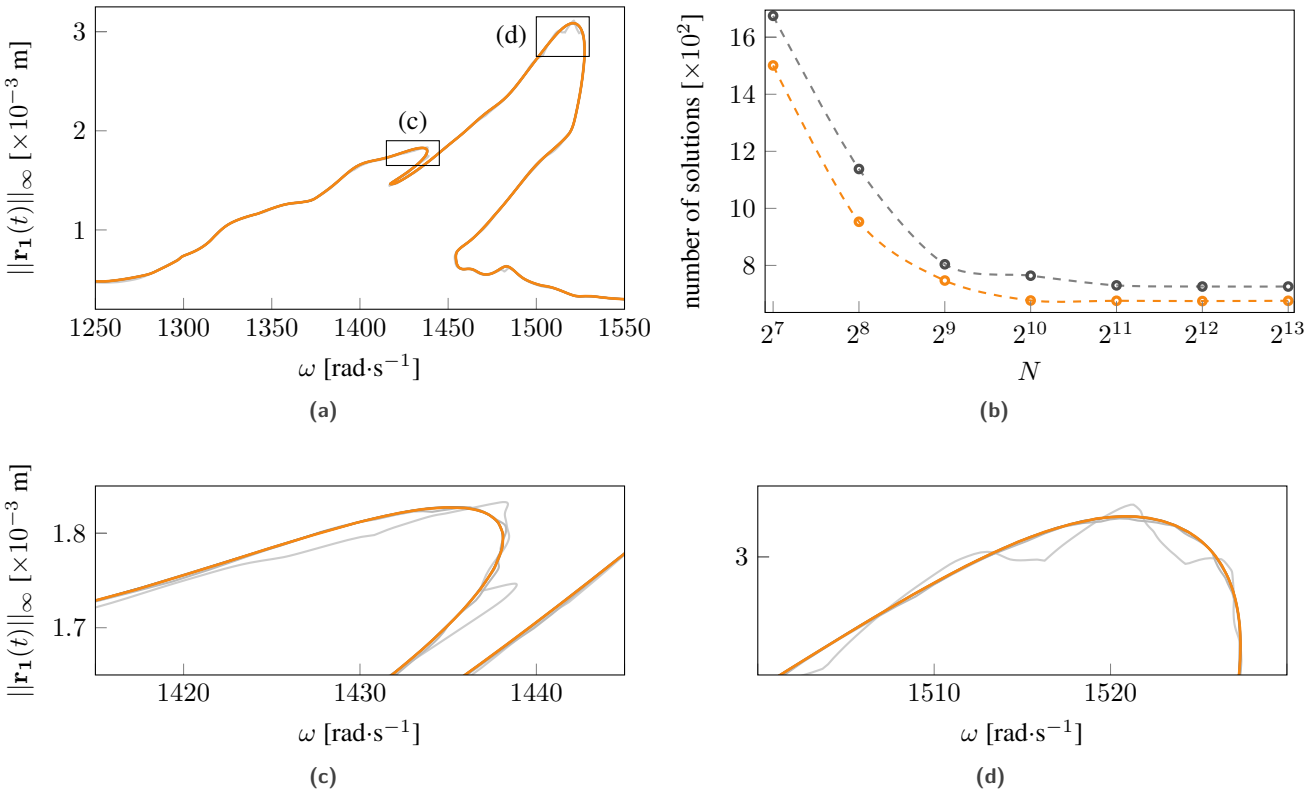


**Figure 18** – NFRC computed with RL-HBM ($H = 40$) for $N = \{2^7 = 128$ (——), 256 (——), 512 (——), 1024 (——), 2048 (——), $2^{13} = 4096$ (——)$\}$ (a) full NFRC, (b) number of the NFRC solutions points with (-o-) and without (-o-) Lanczos filtering, (c) zoom over the turning area and (d) nonlinear resonance.

number of solution points over the NFRC.

### 4.5.2 NFRC analysis

The NFRC obtained with the proposed RL-HBM are respectively depicted in Fig. 19a for the blade's leading edge (LE) and in Fig. 19b for the blade's trailing edge (TE). Corresponding TI reference solutions are plotted on the same figures for the sake of comparison. There is, overall, a very good agreement between the results obtained with TI and the proposed methodology. It is first remarkable how the nonlinear resonance predicted with the proposed methodology ($\omega_{rnl} \simeq 1525$ rad·s$^{-1}$) is far higher than the one predicted with the TI reference solution ($\omega_{rnl} \simeq 1448$ rad·s$^{-1}$). With respect to the linear resonance expected for $\omega_r = 1320$ rad·s$^{-1}$ (intersection between the fourth engine order and the first bending mode, see Fig. 1), this implies a 67 % increase of the resonance frequency shift. Besides of the actual nonlinear resonance angular frequency shift, a key element for blade designers lies in the fact that maximum vibration amplitudes predicted by TI reference solutions are about 59 % lower than those obtained with the RL-HBM.

Noticeable differences are found between the evolution of the vibration amplitudes at LE and TE. In particular, the solution branch between ④ and ⑤ in Fig. 19 is found to be significantly smoother at TE. This is a good indication that the variations observed at LE are not related to numerical artifacts (which is confirmed by the fact that a perfect superimposition of the NCRF was also observed for higher values of $H$ and $N$). Interestingly, the angular frequency for which the maximal vibration amplitude is evidenced at LE, see area ⑤ in Fig. 19a, is slightly lower than the one corresponding to the maximal vibration amplitude at TE. These observations underline the intricate dynamic behavior of the investigated blade when subjected to structural contacts.

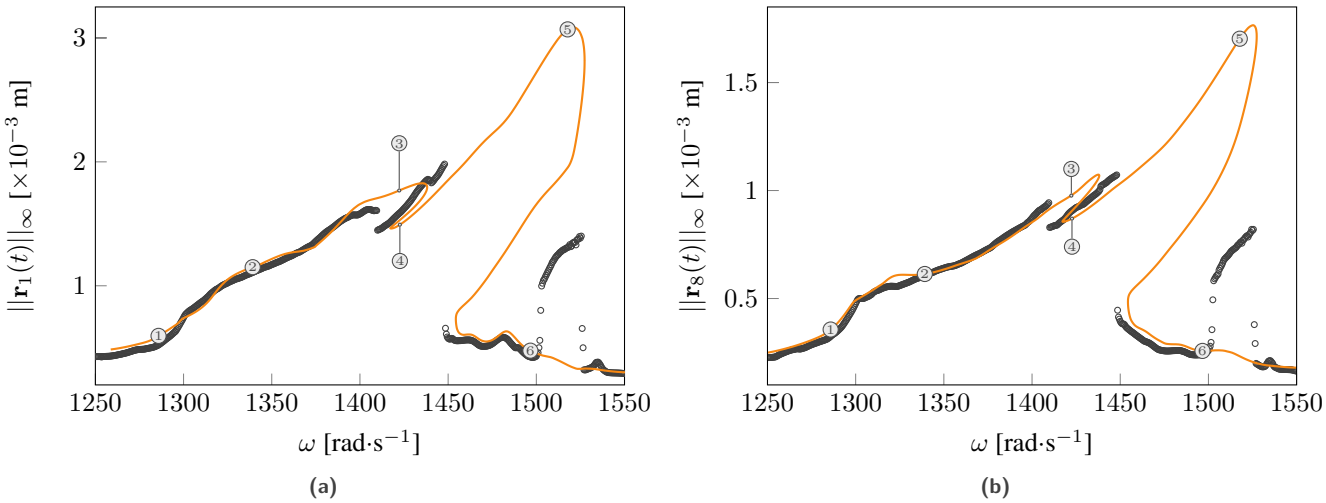


**Figure 19** – NFRC of radial displacements obtained with TI (○) and RL-HBM (——) at (a) LE and (b) TE.

Harmonic contributions of radial displacements at both leading and trailing edges are depicted in Fig. 20 using a logarithmic scale. For the sake of clarity, only the first twelve harmonics are plotted. The $j$-th harmonic contribution regarding the $i$-th dof is evaluated as follows:

$$||H_j^i||_2 = \begin{cases} |a_0^i|/2 & \text{for } j = 0 \\ \sqrt{{a_j^i}^2 + {b_j^i}^2} & \text{for } j \in [\![1\,..\,H]\!] \end{cases} \tag{48}$$

These results underline that only even harmonics respond, which is consistent with the fact that the contact configuration features two evenly spaced lobes on the casing surface. This was also evidenced with TI results in the interaction map depicted in Fig. 1a.

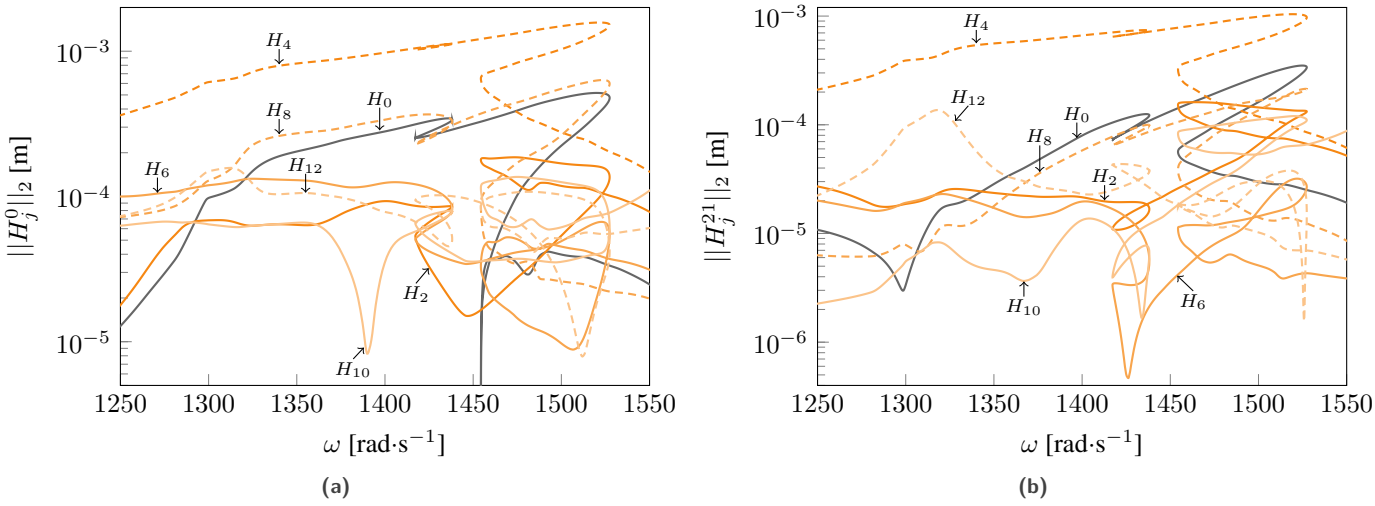


**Figure 20** – Harmonics contribution for RL-HBM radial displacements solutions at (a) LE and (b) TE: $H_0$ (——), $H_2$ (——), $H_4$ (- - -), $H_6$ (——), $H_8$ (- - -), $H_{10}$ (——) and $H_{12}$ (- - -).

There is, however, an area for which the TI reference strategy and the RL-HBM do not seem to provide similar

results. This is patent in the lower branch of solutions for $\omega \in [1500,\ 1525]$ rad·s$^{-1}$. Indeed, in this region TI reference solutions feature much higher amplitudes. An in-depth analysis of this last area is carried out later in this section.

In order to assess more quantitatively the accuracy of the results obtained with the RL-HBM, several areas—marked ① to ⑥ in Fig. 19, see Tab. 1—are considered for an in-depth comparative analysis with a two-pronged approach. (1) Where predicted amplitudes with both methodologies are found to be very close (areas ①, ② and ④), displacements, contact forces and velocities are directly superimposed. Otherwise, (2) areas where the proposed methodology reveals an intricated dynamical behavior (areas ③ and ⑥) or where predicted amplitudes may not match between TI and the RL-HBM (areas ③ and ⑤), TI reference simulations are re-run using initial conditions directly taken from the RL-HBM solution, subsequent results are then superimposed to the RL-HBM results.

| area | ① | ② | ③ | ④ | ⑤ | ⑥ |
|---|---|---|---|---|---|---|
| $\omega$ [rad·s$^{-1}$] | 1285.823 | 1339.193 | 1422.277 | 1422.643 | 1517.767 | 1496.641 |

**Table 1** – Considered angular frequencies.

Finally, the influence of the damping coefficients used for the different vibration modes of the blade has been assessed. While an in-depth investigation on damping would go beyond the scope of this paper, it was found that damping coefficients in the vicinity of commonly accepted values for aircraft engine blades (typical values of damping coefficients for the first two free-vibration modes—bending and torsion—range from $5 \cdot 10^{-4}$ to $2 \cdot 10^{-3}$) had low influence on the nonlinear resonance, be it in terms of frequency or amplitude. It is assumed that this phenomenon is related to the forced nature of the contact interaction combined with the lack of external excitation on the blade. This is however an important result as it confirms that presented results do not significantly depend on these damping coefficients and that the proposed methodology remains well-suited for low damping values.

#### 4.5.3 Displacements and contact forces

Displacements and contact forces obtained with both methodologies in areas ① to ⑥ are depicted in Figs 21 and 22. In each subfigure, dark colors are used for quantities related to the leading edge while lighter colors are used for quantities related to the trailing edge. The blade twist angle implies an angular shift between these two points which explains why the casing lobes appear at slightly different locations in the displacement plots. Looking at both displacements and contact forces for any of the six investigated areas, there is a very good agreement between the results obtained with the two numerical strategies. Despite of the severity of the contact configuration, there is almost no spurious oscillation visible on the results obtained with the RL-HBM. This highlights the benefits of the employed Lanczos filtering technique to mitigate the Gibbs phenomenon.

The only non negligible discrepancies between the TI reference solutions and the results of the RL-HBM are related to the contact forces, particularly in Figs. 21f, 22d and 22e. It is interesting to note that these discrepancies do not translate into significant errors on the predicted displacements. It is assumed that the origin of these discrepancies lies in the fact that two very distinct contact treatment algorithms (Lagrange multipliers / regularized penalty method) are employed. Nonetheless, and similarly to what was observed on the rod test case, the obtained results overall confirm the fairly low sensitivity of the results to the contact treatment algorithm.

The excellent agreement in area ⑤ is worth underlining as it demonstrates that the predicted nonlinear resonance with the RL-HBM—a solution that was not initially obtained with the TI reference strategy—may indeed be obtained with TI when using the proper set of initial conditions. Though a stability analysis, that could be carried out applying Floquet theory in the time domain by computing the monodromy matrix [50] or in the frequency domain with Hill's method [51], would go beyond the scope of this article, the solution is likely to be stable since the set of initial conditions are associated to a different contact treatment procedure than the one employed with the TI reference strategy.

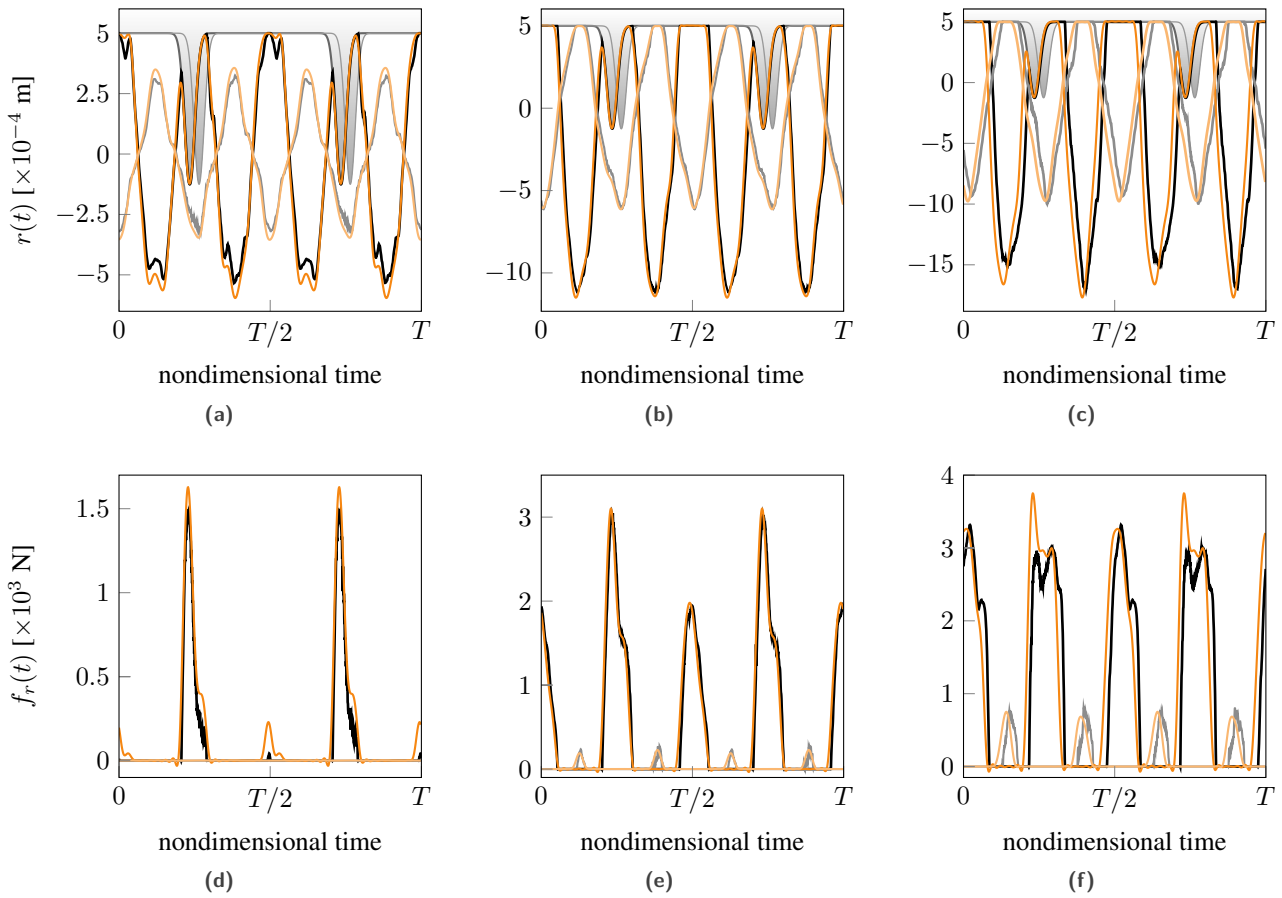


**Figure 21** – Comparison between radial displacements and contact forces obtained by RL-HBM and TI at LE and TE for areas: (a) (d) ①, (b) (e) ②, and (c) (f) ③. Legends: TI LE (——), TE (——), RL-HBM LE (——) and TE (——).

#### 4.5.4 Velocities

Velocities of both LE and TE obtained with the TI reference strategy and the RL-HBM are pictured in Fig. 23. Here again, there is a very good agreement between the two employed numerical strategies. The sensitivity of the computation of velocities to the time step for TI, combined with the prediction/correction contact treatment procedure, actually yields spurious oscillations of the reference signals. In this context, the signals obtained with the RL-HBM actually look smoother, with minimal oscillations in the vicinity of the contact areas.

#### 4.5.5 Stress fields

For each of the six investigated areas, the focus is made on the time where the radial displacement is maximal, considering every boundary nodes. For each of these areas, the maximal displacement is always found at the blade's leading edge. At each of these six instants, the blade displacement fields obtained with the TI reference strategy and the RL-HBM are deployed from the reduced space back onto the full finite element model in order to compute the corresponding von Mises stress fields. These stress fields are all depicted in Fig. 24. For each stress field, the maximal computed stress is indicated as a fraction of the blade's material yield stress $\sigma_Y$. There is an excellent agreement between the stress fields obtained with both methodologies. In complement with the observations previously made on the LE and TE displacements, these observations confirm that the results obtained with the RL-HBM are very

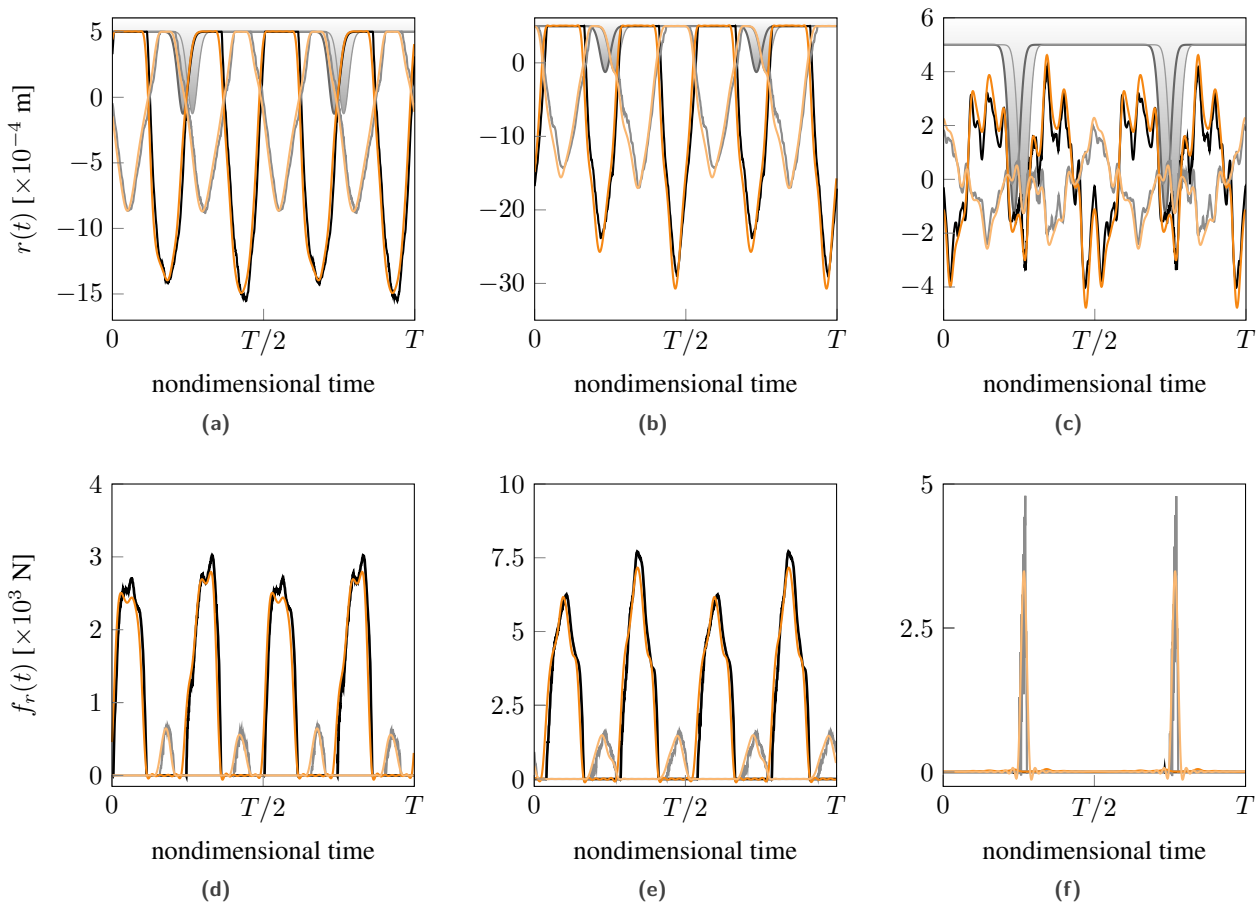


**Figure 22** – Comparison between radial displacements and contact forces obtained by RL-HBM and TI at LE and TE for areas: (a) (d) ④, (b) (e) ⑤, and (c) (f) ⑥. Legends: TI LE (——), TE (——), RL-HBM LE (——) and TE (——).

accurate, both for the nonlinear interface and the modal coefficients that are key to retrieve accurate stress fields.

From a physical standpoint, it is interesting to see that the considered contact configuration is extremely severe as resulting stress levels in the blade far exceed the blade material's yield stress close to the nonlinear resonance, see stress fields in Figs. 24i and 24j. This is an important observation as it underlines that the RL-HBM is robust enough to provide converged results even for such severe contact configurations.

#### *4.5.6 Areas of discrepancy*

As mentioned above, there are significant discrepancies between the results provided by the TI reference solution and the RL-HBM in the lower branch of solutions for $\omega \in [1500,\ 1525]$ rad·s$^{-1}$ rad·s$^{-1}$ in Fig. 19. Over this angular speed range, particular attention should be paid as the RL-HBM fails to capture high amplitude solutions that could be detrimental to the blade's lifespan. To this end, the radial displacement of the blade's LE predicted with the TI reference strategy is plotted in Fig. 25a over the last six revolutions of the simulation. The frequency spectrum of this time signal is depicted next to it, in Fig. 25b.

A close inspection of the spectrum in Fig. 25b reveals that only a small portion of the signal's harmonic content lies on the harmonics retained in the RL-HBM strategy (see the grey lines in Fig. 25b). This is key for understanding why the RL-HBM fails to capture this solution. Interestingly, the time signal depicted in Fig. 25a actually features a

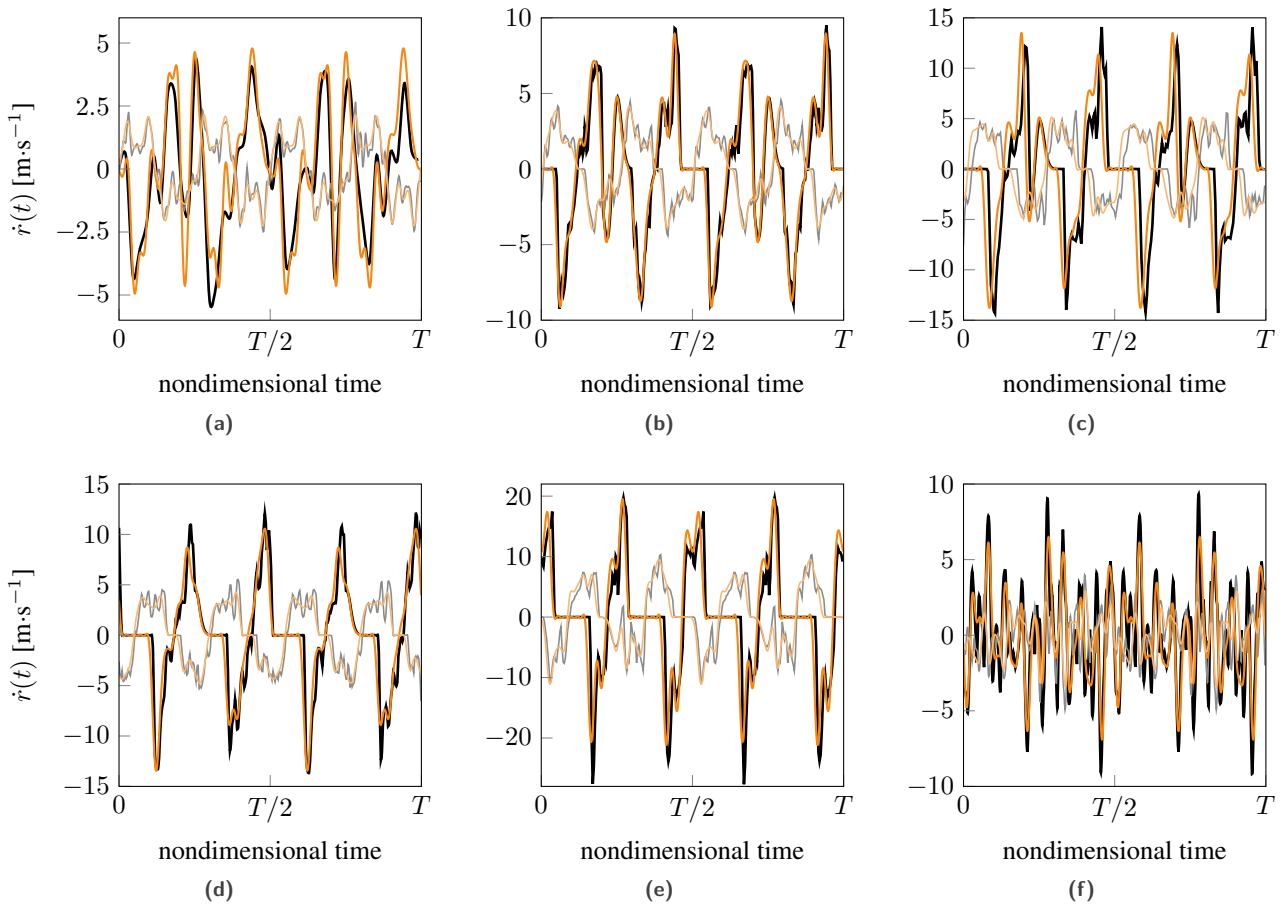


**Figure 23** – Comparison between radial velocities obtained by RL-HBM and TI at LE and TE for areas: (a) ①, (b) ②, (c) ③, (d) ④, (e) ⑤ and (f) ⑥. Legends: TI LE (——), TE (——), RL-HBM LE (——) and TE (——).

period that is 13.5 times greater than the blade's period of revolution $T$. Though capturing such type of solution with the RL-HBM is theoretically conceivable, it would imply considering a subharmonic ratio ($\nu = 27$) [18] that would multiply the size of the Fourier basis to $n_b(2\nu H + 1)$. The cost in terms of computation times would simply be unacceptable with current computing resources.

### *4.5.7 Discussion*

To the best of the author's knowledge, this is the first time that a HBM-based methodology is applied for the analysis of the vibration behavior of an industrial structure impacting a rigid obstacle. The two-pronged approach for the mitigation of spurious oscillations due to the Gibbs phenomenon is found to be very efficient on two distinct mechanical systems undergoing very severe unilateral contact constraints: an academic rod with a single nonlinear dof and an industrial compressor blade with 24 nonlinear dof. Indeed, convergence issues that have been observed for both systems with the HBM—and that become critical in the case of the industrial blade with a moving obstacle—completely vanish with the RL-HBM.

Interestingly, results obtained with the RL-HBM—considering a penalty-based contact treatment algorithm—are overall very coherent with those obtained with the TI reference strategy—relying on a Lagrange multiplier-based contact treatment algorithm. To some extent, this is unexpected as it was initially assumed that a penalty-based approach may not be able to accurately predict contact forces for a wide angular speed range over which vibration and

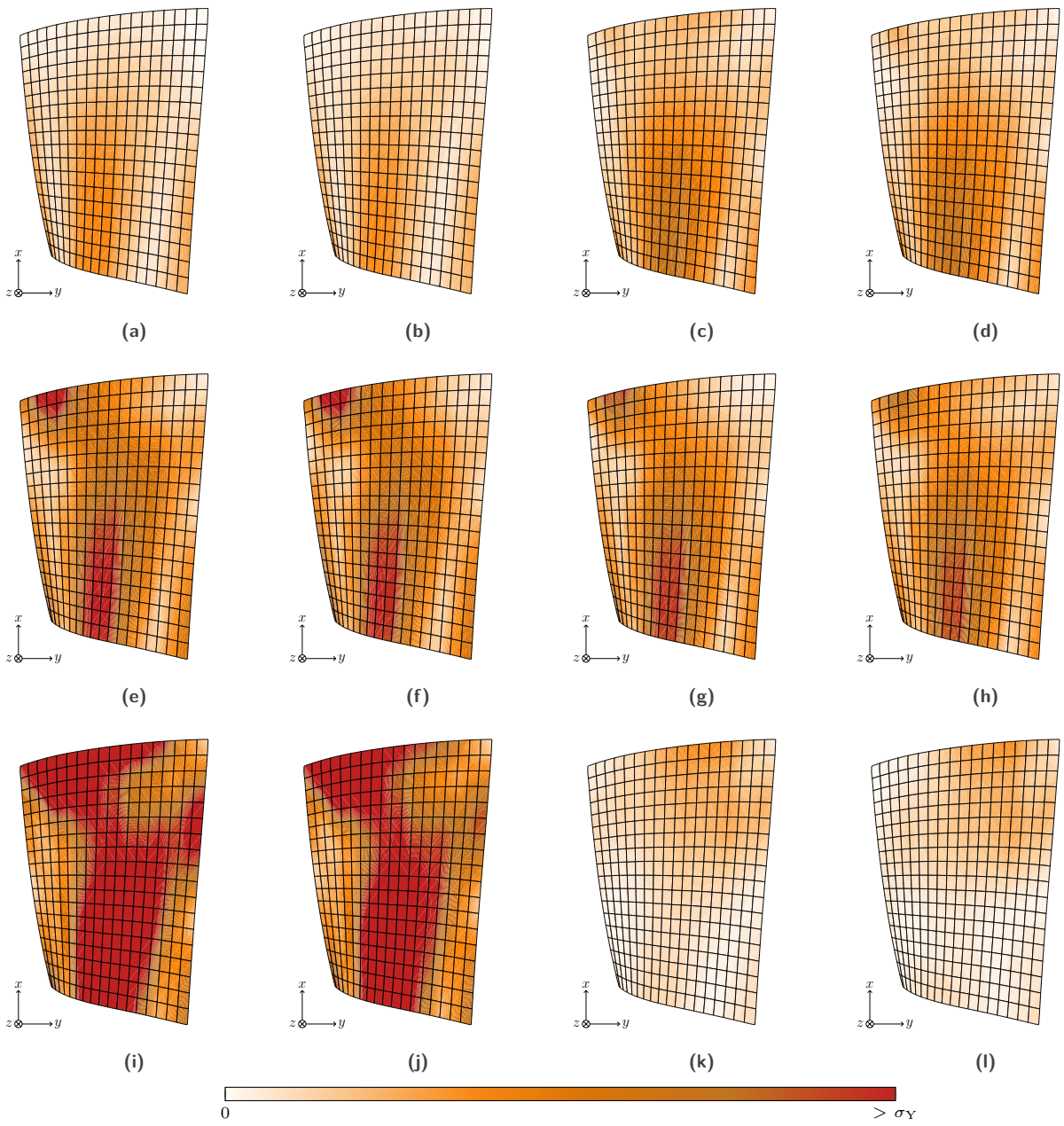


**Figure 24** – Comparison between resulting von Mises stress obtained with RL-HBM and TI at corresponding HBM maximal displacement instant. RL-HBM for areas: (a) ① $\sigma_{max} = 0.429\,\sigma_Y$, (c) ② $\sigma_{max} = 0.777\,\sigma_Y$, (e) ③ $\sigma_{max} = 1.012\,\sigma_Y$, (g) ④ $\sigma_{max} = 0.941\,\sigma_Y$, (i) ⑤ $\sigma_{max} = 1.674\,\sigma_Y$ and (k) ⑥ $\sigma_{max} = 0.406\,\sigma_Y$. TI for areas: (b) ① $\sigma_{max} = 0.404\,\sigma_Y$, (d) ② $\sigma_{max} = 0.767\,\sigma_Y$, (f) ③ $\sigma_{max} = 0.993\,\sigma_Y$, (h) ④ $\sigma_{max} = 0.91\,\sigma_Y$, (j) ⑤ $\sigma_{max} = 1.587\,\sigma_Y$ and (l) ⑥ $\sigma_{max} = 0.425\,\sigma_Y$.

contact force amplitudes greatly vary. On the one hand, this observation suggests that the analysis of blade-tip/casing contacts may be accurately carried out with a penalty-based approach thus yielding more efficient time integration

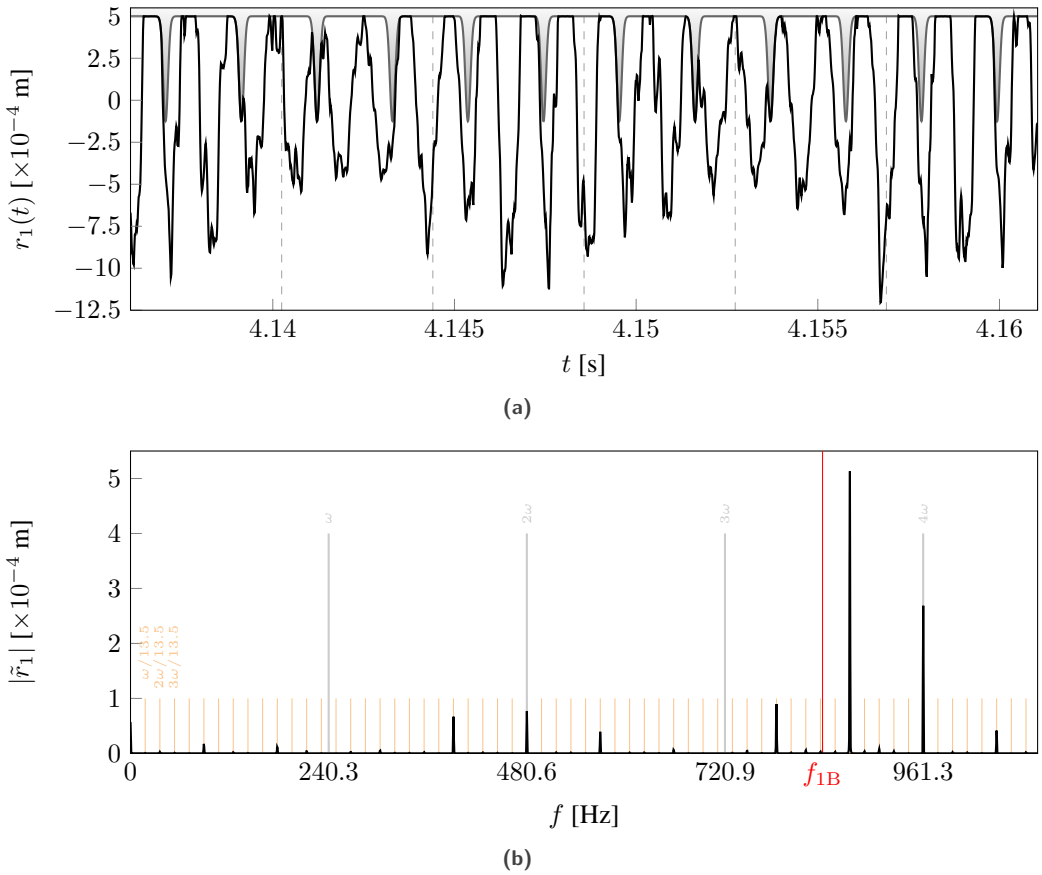


**Figure 25** – 13.5-$T$-periodic solution obtained with TI at $\omega = 1510$ rad·s$^{-1}$: (a) displacements over revolutions 995 to 1000 and (b) FFT frequency spectrum.

simulations. On the other hand, using a penalty-based approach does require a potentially costly *a priori* numerical investigation in order to assess a meaningfull value of both the stiffness coefficient $\kappa$ and the regularization parameter $\gamma$.

When looking at the pros and cons of each of the two considered solution paradigms (time integration/frequency methods), this study underlines that they actually complement each other. For the considered industrial application, considering only time integration simulations would yield a very significant error on the prediction of the nonlinear resonance. However, considering only frequency methods would make it impossible to capture specific solutions which periods spread over several blade revolutions. Finally, time integration simulations are oftentimes presented as more computationally expensive than HBM simulations. This argument becomes questionable when considering industrial mechanical systems with a large number of dof. As a matter of fact, computation times for the TI reference strategy and for the RL-HBM to obtain the results depicted in Figs. 19a and 19b are of comparable magnitude.

## 5 Conclusion

In this paper, a harmonic balance method-based numerical methodology is introduced for the analysis of blade-tip/casing contact interactions in aircraft engines. It aims at providing the missing qualitative counterpart to quantitative results obtained by existing time integration numerical strategies. The proposed methodology focuses on the mitigation of spurious oscillations related to the Gibbs phenomenon and that arise when using the harmonic balance method for the analysis of nonlinear mechanical systems. This methodology is successfully applied to two

distinct mechanical systems undergoing contact constraints: a cantilever rod and an industrial compressor blade. As a first step towards the development of a frequency method strategy for the analysis of rubbing interactions in aircraft engines, centrifugal stiffening and casing wear are not accounted for. The accuracy of the proposed methodology is demonstrated through its validation with respect to an already published time integration-based reference numerical strategy. This underlines that frequency methods can be efficiently used for the prediction of blade-tip/casing contacts. Indeed, Displacements, contact forces, velocities and stress fields are predicted in very good agreement with the reference numerical strategy. This paper also highlights the intricacy of a blade's dynamics undergoing structural contacts, to a point where both time domain and frequency domain solution paradigms are needed to capture all potentially harmful interactions. The proposed methodology advantageously captures the blade's nonlinear resonance, which may not be found with time integration-based strategies. To the contrary, time integration-based strategies can predict solutions with intricated frequency content that would be extremely costly to compute with frequency methods.

## Acknowledgment

This research was supported by the Natural Sciences and Engineering Research Council of Canada (NSERC).

## References

[1] Padova, C., Barton, J., Dunn, M. G., and Manwaring, S., 2006. "Experimental results from controlled blade tip/shroud rubs at engine speed". *J. Turbomach.,* **129**(4), pp. 713–723. doi: 10.1115/1.2720869 - oai: hal-01333702v1.

[2] Vernet, N., Ruiz, E., Advani, S., Alms, J., Aubert, M., Barburski, M., Barari, B., Beraud, J., Berg, D., Correia, N., Danzi, M., Delavière, T., Dickert, M., Di Fratta, C., Endruweit, A., Ermanni, P., Francucci, G., Garcia, J., George, A., Hahn, C., Klunker, F., Lomov, S., Long, A., Louis, B., Maldonado, J., Meier, R., Michaud, V., Perrin, H., Pillai, K., Rodriguez, E., Trochu, F., Verheyden, S., Wietgrefe, M., Xiong, W., Zaremba, S., and Ziegmann, G., 2014. "Experimental determination of the permeability of engineering textiles: Benchmark ii". *Compos. Part A: Appl. Sci. Manuf.,* **61**, pp. 172–184. doi: 10.1016/j.compositesa.2014.02.010.

[3] Nyssen, F., Tableau, N., Lavazec, D., and Batailly, A., 2020. "Experimental and numerical characterization of a ceramic matrix composite shroud segment under impact loading". *J. Sound Vib.,* **467**, p. 115040. doi: 10.1016/j.jsv.2019.115040 - oai: hal-02378746.

[4] Investigation: 200700356 - In-flight engine failure, Sydney, 03 February 2007, Boeing Company 747-438, VH-OJM. Tech. rep., Australian Transport Safety Bureau. https://www.atsb.gov.au/publications/investigation_reports/2007/aair/aair200700356, 2008 (accessed 2020-10-29).

[5] Batailly, A., Legrand, M., Millecamps, A., and Garcin, F., 2012. "Numerical-experimental comparison in the simulation of rotor/stator interaction through blade-tip/abradable coating contact". *J. Eng. Gas Turbines Power,* **134**(8), p. 11. doi: 10.1115/1.4006446 - oai: hal-00746632.

[6] Almeida, P., Gibert, C., Thouverez, F., Leblanc, X., and Ousty, J.-P., 2016. "Numerical analysis of bladed disk–casing contact with friction and wear". *J. Eng. Gas Turbines Power,* **138**(12), p. 11. doi: 10.1115/1.4033065.

[7] Thorin, A., Guérin, N., Legrand, M., Thouverez, F., and Almeida, P., 2018. "Nonsmooth Thermoelastic Simulations of Blade–Casing Contact Interactions". *J. Eng. Gas Turbines Power,* **141**(2), p. 7. doi: 10.1115/1.4040857 - oai: hal-01989188.

[8] Petrov, E. P., and Ewins, D. J., 2004. "Generic Friction Models for Time-Domain Vibration Analysis of Bladed Disks". *J. Turbomach.,* **126**(1), pp. 184–192. doi: 10.1115/1.1644557.

[9] Williams, R. J., 2011. "Simulation of Blade Casing Interaction Phenomena in Gas Turbines Resulting From Heavy Tip Rubs Using an Implicit Time Marching Method". In Proceedings of the ASME Turbo Expo 2011, Vol. Volume 6: Structures and Dynamics, Parts A and B, pp. 1007–1016. doi: 10.1115/GT2011-45495 - oai: hal-01555287.

[10] Millecamps, A., Batailly, A., Legrand, M., and Garcin, F., 2015. "Snecma's Viewpoint on the Numerical and Experimental Simulation of Blade-Tip/Casing Unilateral Contacts". In Proceedings of the ASME Turbo Expo 2015, Vol. Volume 7B: Structures and Dynamics. doi: 10.1115/GT2015-42682.

[11] Lesaffre, N., Sinou, J.-J., and Thouverez, F., 2007. "Contact analysis of a flexible bladed-rotor". *Eur. J. Mech. A/Solids,* **26**(3), pp. 541–557. doi: 10.1016/j.euromechsol.2006.11.002 - oai: hal-00322887.

[12] Millecamps, A., Brunel, J.-F., Dufrénoy, P., Garcin, F., and Nucci, M., 2009. "Influence of thermal effects during blade-casing contact experiments". In Proceedings of the ASME IDETC/CIE 2009, pp. 855–862. doi: 10.1115/DETC2009-86842 - oai: hal-01223060.

[13] Batailly, A., Agrapart, Q., Millecamps, A., and Brunel, J.-F., 2016. "Experimental and numerical simulation of a rotor/stator interaction event localized on a single blade within an industrial high-pressure compressor". *J. Sound Vib.,* **375**, pp. 308–331. doi: 10.1016/j.jsv.2016.03.016 - oai: hal-01342401.

[14] Ma, H., Yin, F., Wu, Z., Tai, X., and Wen, B., 2016. "Nonlinear vibration response analysis of a rotor-blade system with blade-tip rubbing". *Nonlinear Dyn.,* **84**(3), pp. 1225–1258. doi: 10.1007/s11071-015-2564-5.

[15] Almeida, P., Gibert, C., Thouverez, F., Leblanc, X., and Ousty, J.-P., 2015. "Experimental analysis of dynamic interaction between a centrifugal compressor and its casing". *J. Turbomach.,* **137**(3), p. 031008. doi: 10.1115/1.4028328 - oai: hal-01574149.

[16] Yoong, C., Thorin, A., and Legrand, M., 2018. "Nonsmooth modal analysis of an elastic bar subject to a unilateral contact constraint". *Nonlinear Dyn.,* **91**(4), pp. 2453–2476. doi: 10.1007/s11071-017-4025-9 - oai: hal-01471341.

[17] Carpenter, N. J., Taylor, R. L., and Katona, M. G., 1991. "Lagrange constraints for transient finite element surface contact". *Int. J. Numer. Methods Eng.,* **32**(1), pp. 103–128. doi: 10.1002/nme.1620320107 - oai: hal-01389918.

[18] Von Groll, G., and Ewins, D. J., 2001. "The harmonic balance method with arc-length continuation in rotor/stator contact problems". *J. Sound Vib.,* **241**(2), pp. 223–233. doi: 10.1006/jsvi.2000.3298 - oai: hal-01333704.

[19] Petrov, E. P., 2011. "A High-Accuracy Model Reduction for Analysis of Nonlinear Vibrations in Structures With Contact Interfaces". *J. Eng. Gas Turbines Power,* **133**(10), p. 10. doi: 10.1115/1.4002810.

[20] Krack, M., Panning-von Scheidt, L., and Wallaschek, J., 2016. "On the interaction of multiple traveling wave modes in the flutter vibrations of friction-damped tuned bladed disks". *J. Eng. Gas Turbines Power,* **139**(4), p. 9. doi: 10.1115/1.4034650.

[21] Krack, M., Salles, L., and Thouverez, F., 2017. "Vibration prediction of bladed disks coupled by friction joints". *Arch. Comput. Methods Eng.,* **24**(3), pp. 589–636. doi: 10.1007/s11831-016-9183-2 - oai: hal-01825517.

[22] Petrov, E. P., 2012. "Multiharmonic analysis of nonlinear whole engine dynamics with bladed disc-casing rubbing contacts". In Proceedings of the ASME Turbo Expo 2012, Vol. Volume 7: Structures and Dynamics, Parts A and B, pp. 1181–1191. doi: 10.1115/GT2012-68474.

[23] Salles, L., Staples, B., Hoffmann, N., and Schwingshackl, C., 2016. "Continuation techniques for analysis of whole aeroengine dynamics with imperfect bifurcations and isolated solutions". *Nonlinear Dyn.,* **86**, pp. 1897–1911. doi: 10.1007/s11071-016-3003-y.

[24] Jerri, A. J., 1998. *The Gibbs Phenomenon in Fourier Analysis, Splines and Wavelet Approximations*, Vol. 446. Springer, Boston, MA. doi: 10.1007/978-1-4757-2847-7.

[25] Meingast, M. B., Legrand, M., and Pierre, C., 2014. "A linear complementarity problem formulation for periodic solutions to unilateral contact problems". *Int. J. Non-Linear Mech.,* **66**, pp. 18–27. doi: 10.1016/j.ijnonlinmec.2014.01.007 - oai: hal-00955647v1.

[26] Jones, S., and Legrand, M., 2014. "Forced vibrations of a turbine blade undergoing regularized unilateral contact conditions through the wavelet balance method". *Int. J. Numer. Methods Eng.,* **101**(5), pp. 351–374. doi: 10.1002/nme.4807 - oai: hal-00806545.

[27] Batailly, A., Legrand, M., Millecamps, A., Cochon, S., and Garcin, F., 2015. "Redesign of a high-pressure compressor blade accounting for nonlinear structural interactions". *J. Eng. Gas Turbines Power,* **137**(2), p. 8. doi: 10.1115/1.4028263 - oai: hal-01120158.

[28] Allgower, E. L., and Georg, K., 1990. *Introduction to numerical continuation methods*, Vol. 13. Springer, Berlin, Heidelberg. doi: 10.1007/978-3-642-61257-2.

[29] Woiwode, L., Narayanaa Balaji, N., Kappauf, J., Tubita, F., Guillot, L., Vergez, C., Cochelin, B., Grolet, A., and Krack, M., 2020. "Comparison of two algorithms for harmonic balance and path continuation". *Mech. Syst. Signal Process.,* **136**, p. 106503. doi: 10.1016/j.ymssp.2019.106503 - oai: hal-02424746.

[30] Cardona, A., Lerusse, A., and Géradin, M., 1998. "Fast Fourier nonlinear vibration analysis". *Comput. Mech.,* **22**(2), pp. 128–142. doi: 10.1007/s004660050347.

[31] Seydel, R., 2009. *Practical bifurcation and stability analysis*, Vol. 5. Springer, New York. doi: 10.1007/978-1-4419-1740-9.

[32] Keller, H. B., 1983. "The bordering algorithm and path following near singular points of higher nullity". *SIAM J. Sci. and Stat. Comput.,* **4**(4), pp. 573–582. doi: 10.1137/0904039.

[33] Govaerts, W. J. F., 2000. *Numerical Methods for Bifurcations of Dynamical Equilibria.* SIAM. doi: 10.1137/1.9780898719543.

[34] Cameron, T. M., and Griffin, J. H., 1989. "An alternating frequency/time domain method for calculating the steady-state response of nonlinear dynamic systems". *J. Appl. Mech.,* **56**(1), pp. 149–154. doi: 10.1115/1.3176036 - oai: hal-01333697.

[35] Narayanan, S., and Sekar, P., 1998. "A frequency domain based numeric–analytical method for non-linear dynamical systems". *J. Sound Vib.,* **211**(3), pp. 409–424. doi: 10.1006/jsvi.1997.1319.

[36] Sarrouy, E., and Sinou, J.-J., 2011. "Non-linear periodic and quasi-periodic vibrations in mechanical systems - on the use of the harmonic balance methods". In *Advances in Vibration Analysis Research*, F. Ebrahimi, ed. IntechOpen, Rijeka, ch. 21, pp. 419–434. doi: 10.5772/15638 - oai: hal-00730895.

[37] Krack, M., and Gross, J., 2019. *Harmonic Balance for Nonlinear Vibration Problems.* Springer, Cham. doi: 10.1007/978-3-030-14023-6.

[38] Schreyer, F., and Leine, R. I., 2016. "A mixed shooting – harmonic balance method for unilaterally constrained mechanical systems". *Arch. Mech. Eng.,* **vol. 63**(No 2), pp. 297–314. doi: 10.1515/meceng-2016-0017 - oai: hal-01356796v1.

[39] Kim, W.-J., and Perkins, N., 2003. "Harmonic balance/galerkin method for non-smooth dynamic systems". *J. Sound Vib.,* **261**(2), pp. 213–224. doi: 10.1016/S0022-460X(02)00949-5 - oai: hal-01693093v1.

[40] Gelb, A., and Gottlieb, S., 2007. "The resolution of the gibbs phenomenon for fourier spectral methods". In *Advances in The Gibbs Phenomenon. 1st edition (2011).* Sampling Publishing. Potsdam, New York., ch. 7. ISBN : 0967301-0-8.

[41] Wriggers, P., and Laursen, T. A., 2007. *Computational Contact Mechanics*, Vol. 498. Springer, Vienna. doi: 10.1007/978-3-211-77298-0.

[42] Nacivet, S., Pierre, C., Thouverez, F., and Jezequel, L., 2003. "A dynamic Lagrangian frequency–time method for the vibration of dry-friction-damped systems". *J. Sound Vib.,* **265**(1), pp. 201–219. doi: 10.1016/S0022-460X(02)01447-5 - oai: hal-01635272.

[43] Djeddi, R., and Ekici, K., 2016. "Resolution of gibbs phenomenon using a modified pseudo-spectral operator in harmonic balance cfd solvers". *Int. J. Comput. Fluid Dyn.,* **30**(7-10), pp. 495–515. doi: 10.1080/10618562.2016.1242726.

[44] Legrand, M., Batailly, A., Magnain, B., Cartraud, P., and Pierre, C., 2012. "Full three-dimensional investigation of structural contact interactions in turbomachines". *J. Sound Vib.,* **331**(11), pp. 2578–2601. doi: 10.1016/j.jsv.2012.01.017 - oai: hal-00660863.

[45] Craig Jr, R. R., and Bampton, M. C. C., 1968. "Coupling of substructures for dynamic analyses". *AIAA J.,* **6**(7), pp. 1313–1319. doi: 10.2514/3.4741.

[46] Batailly, A., Legrand, M., Cartraud, P., and Pierre, C., 2010. "Assessment of reduced models for the detection of modal interaction through rotor stator contacts". *J. Sound Vib.,* **329**(26), pp. 5546–5562. doi: 10.1016/j.jsv.2010.07.018 - oai: hal-00524762v1.

[47] Reid, L., and Moore, R. D. Design and overall performance of four highly loaded, high speed inlet stages for an advanced high-pressure-ratio core compressor. Tech. rep., NASA Lewis Research Center Cleveland, OH, United States. https://ntrs.nasa.gov/citations/19780025165, 1978 (accessed 2020-10-29).

[48] Piollet, E., Nyssen, F., and Batailly, A., 2019. "Blade/casing rubbing interactions in aircraft engines: Numerical benchmark and design guidelines based on nasa rotor 37". *J. Sound Vib.,* **460**, p. 114878. doi: 10.1016/j.jsv.2019.114878 - oai: hal-02281666.

[49] Huebler, D. Rotor 37 and stator 37 assembly. Records of the National Aeronautics and Space Administration, 1903 - 2006. Photographs relating to agency activities, facilities and personnel, 1973 - 2013. https://catalog.archives.gov/id/17468361, 1977 (accessed 2020-10-29).

[50] Peletan, L., Baguet, S., Torkhani, M., and Jacquet-Richardet, G., 2013. "A comparison of stability computational methods for periodic solution of nonlinear problems with application to rotordynamics". *Nonlinear Dyn.,* **72**(3), pp. 671–682. doi: 10.1007/s11071-012-0744-0 - oai: hal-00813265v1.

[51] Bentvelsen, B., and Lazarus, A., 2018. "Modal and stability analysis of structures in periodic elastic states: application to the ziegler column". *Nonlinear Dyn.,* **91**(2), pp. 1349–1370. doi: 10.1007/s11071-017-3949-4 - oai: hal-01686514.